CAPITAL UNIVERSITY OF SCIENCE AND TECHNOLOGY, ISLAMABAD

Neural Network Based Finite Element Approach for Micromagnetorotation Boundary Layer Flow

by

Maryam Ihsan

A thesis submitted in partial fulfillment for the degree of Master of Mathematics

in the

Faculty of Computing
Department of Mathematics

2026

CERTIFICATE OF APPROVAL

Neural Network Based Finite Element Approach for Micromagnetorotation Boundary Layer Flow

by

Maryam Ihsan

(Registration No: MMT243012)

Thesis Evaluation Panel

S. No.	Examiner	Name	Organization
(a)	External Examiner	Dr. Shahzad Munir	COMSATS, Islamabad
(b)	Internal Examiner	Dr. Rida Rafaqat	CUST, Islamabad

Dr. Muhammad Sabeel Khan

Thesis Supervisor

July, 2026

Dr. Muhammad Sagheer

Head, Dept. of Mathematics

July, 2026

Dr. M. Abdul Qadir

Dean, Faculty of Computing

July, 2026

Author's Declaration

I, **Maryam Ihsan**, hereby state that my M.Phil thesis titled **"Neural Network Based Finite Element Approach for Micromagnetorotation Boundary Layer Flow,"** is my own work and has not been submitted previously by me for taking any degree from Capital University of Science and Technology, Islamabad or anywhere else in the country/abroad.

At any time if my statement is found to be incorrect even after my graduation, the University has the right to withdraw my M.Phil Degree.

(Maryam Ihsan)

Registration No. MMT243012

Plagiarism Undertaking

I solemnly declare that the research presented in this thesis titled "**Neural Network Based Finite Element Approach for Micromagnetorotation Boundary Layer Flow**", is solely my research work with no significant contribution from any other person. Small contribution/help whenever taken has been duly acknowledged and that complete thesis has been written by me.

I understand the zero tolerance policy of the HEC and Capital University of Science and Technology towards plagiarism. Therefore, I as an author of the above titled thesis declare that no portion of my thesis has been plagiarized and any material used as reference is properly referred/cited.

I undertake that if I am found guilty of any formal plagiarism in the above titled thesis even after award of MPhil Degree, the University reserves the right to withdraw/revoke my MPhil degree and that HEC and the University have the right to publish my name on the HEC/University website on which names of students are placed who submitted plagiarized work.

(Maryam Ihsan)
Registration No. MMT243012

Acknowledgement

In the name of **ALLAH**, the Most Gracious and Merciful, who blessed humanity with the wisdom and knowledge to explore the mysteries of the universe after bringing it into existence. First and foremost, I would like to express my deepest gratitude to my supervisor, **Dr. Muhammad Sabeel Khan**, for their continuous support, patience, and invaluable guidance throughout the course of this research. Their expertise and encouragement have been instrumental in the completion of this thesis.

I would like to express my deepest gratitude to my parents, whose unconditional love, constant support, and unwavering belief in me have been the foundation of my academic journey. Their sacrifices, encouragement, and guidance have shaped who I am today and have given me the strength to pursue my goals. Thank you for always standing by me, for believing in my dreams, and for being my greatest source of motivation. This thesis is as much yours as it is mine. .

Lastly,I am deeply grateful to my husband **Umar Bin Mazhar** for his continuous support, encouragement, and patience during this research. His belief in me and his understanding during challenging times greatly contributed to the successful completion of this thesis.

(Maryam Ihsan)

Registration No: MMT243012

Abstract

In this thesis, a micromagnetorotative flow model is investigated to analyze heat transfer characteristics within the framework of micropolar fluid theory. The study focuses on flow over a moving liquid surface under the influence of micromagnetorotation (MMR), which naturally arises in micropolar fluids subjected to an externally applied magnetic field. Unlike existing studies, the magnetization-induced microrotational effects are incorporated explicitly into the governing formulation.The resulting nonlinear system of coupled boundary layer equations are solved numerically using a Neural Finite Element Method (Neural FEM). The proposed approach combines the flexibility of finite element discretization with neural network-based learning to obtain stable and accurate solutions. The accuracy of the Neural FEM solutions is validated through comparison with numerical results obtained using the MATLAB `bvp4c` solver by examining key physical quantities such as the skin-friction coefficient and the Nusselt number.The effects of important physical parameters, including the Reynolds number, Prandtl number, micromagnetorotation parameter, and micro-inertial effects, on the flow and thermal fields are examined in detail. The results indicate that an increase in micromagnetorotation significantly reduces the skin-friction coefficient due to enhanced flow uniformity near the surface. Furthermore, the presence of MMR improves the heat transfer rate, leading to higher Nusselt numbers as a result of intensified thermal mixing and thinner thermal boundary layers. The comparative study demonstrates excellent agreement between the Neural FEM and classical numerical solutions, confirming the reliability and effectiveness of the proposed method for solving complex micropolar flow problems.

Contents

List of Figures

List of Tables

List of Abbreviations

CFD	Computational Fluid Dynamics
FEM	Finite Element Method
GFEM	Galerkin Finite Element Method
NFEM	Neural Finite Element Method
NSD	Navier-Stokes/Darcy Model
NSF	Navier-Stokes/Forchheimer Model
NEN	Total Number of Finite Elements
PDE	Partial Differential Equation
PINNs	Physics-Informed Neural Networks

List of Symbols

B	Magnetic induction field
B	Magnetic induction field
B_0	Magnitude of applied magnetic field
$\mathbf{M}$	Magnetization vector
M_0	Magnetization constant
M°	Strength of magnetization
$\mathbf{U}$	Translational velocity vector
$\mathbf{W}$	Micro-rotational velocity vector
u, v	Velocity components
x, y	Cartesian coordinates
F	Dimensionless velocity function
Q	Secondary velocity function
R	Microrotational velocity function
θ	Dimensionless temperature
ξ	Similarity variable
ξ_∞	Far-field boundary
J	Current density
β	Micro-inertial parameter
η_1	Microrotational viscosity
μ_0	Magnetic permeability
ω	Micro-rotational velocity
ω^*	Magnetic relaxation factor
Re	Reynolds number

R_m	Magnetic Reynolds number
Pr	Prandtl number
Ec	Eckert number
Nu	Nusselt number
C_f	Skin-friction coefficient
K	Cosserat (micropolar) number
K_1	Micropolar material parameter
τ_1	Magnetic relaxation time
Ω_0	Surface spin parameter
MMR	Micromagnetorotation parameter
ϵ	Convergence tolerance
p, q, r, s	Missing initial conditions
y_i	First-order system variables
ψ	Stream function
T	Fluid temperature
T_w	Wall temperature
T_∞	Ambient temperature
H_0	Applied magnetic field strength
H_1	Induced magnetic field component in the x-direction
H_2	Magnetic field component in the y-direction
μ	Dynamic viscosity
ν	Kinematic viscosity
k	Vortex (spin) viscosity
ρ	Fluid density
γ^*	Spin-gradient viscosity
κ	Thermal conductivity
C_p	Specific heat at constant pressure
σ	Electrical conductivity
η	Magnetic diffusivity
K	Micropolar (Cosserat) parameter
U_∞	Free-stream velocity

Chapter 1

Introduction and Literature Survey

A computational framework is adopted in this study to determine solutions of nonlinear boundary value problems arising in fluid flow analysis. In this context, a variety of classical numerical techniques have been developed for solving differential equations, among which finite difference and finite element formulations are widely recognized. Shooting methods, in particular, have been extensively utilized due to their favorable convergence behavior and established error characteristics [1, 2]. Within these approaches, the finite element method (FEM) stands out as one of the most versatile and widely implemented techniques. Its popularity is mainly attributed to its capability to effectively model complex geometries, accommodate different types of boundary conditions, and handle strongly coupled transport processes [3, 4].

In recent years, machine learning algorithms and deep neural networks have attracted significant interest as alternative computational frameworks for solving differential equations, offering mesh-free approximations and inherent function approximation capabilities. Physics-Informed Neural Networks (PINNs) enforce the governing equations of the physical system by embedding them within the loss function used during neural network training, enabling the enforcement of differential operators and boundary conditions without classical discretization [5]. By enforcing the residuals of the governing partial differential equations together with the prescribed initial and boundary conditions, PINNs offer a robust and flexible framework for solving both forward and inverse problems in fluid flow and heat transfer [6, 7]. Beyond PINNs, several hybrid and neural finite element formulations have been proposed to address the limitations of both traditional FEM and neural approaches. Early work on finite element neural networks (FENNs) demonstrated that embedding finite element structures within neural network architectures can produce solutions comparable to conventional FEM while leveraging the parallelism and generalization of neural networks [8, 9]. Such hybrid methodologies combine the spatial discretization strengths of FEM with neural network learning, enabling efficient treatment of complex boundary value problems. More recent studies have extended this idea by coupling PINN frameworks with finite element discretizations or basis functions to improve accuracy, enforce boundary conditions more strongly, and handle multidimensional and nonlinear PDEs [10]. Comparative research between physics-informed neural networks and classical FEM solvers has underlined the potential of neural methods to capture complex solution features, although challenges in computational cost and optimization remain [11]. For example, while PINNs can approximate solutions without explicit mesh generation, FEM often retains advantages in accuracy and computational efficiency for well-posed classical problems. Thus, hybrid neural finite element approaches strive to exploit the best of both worlds by combining the neural network approximator with variational or Galerkin formulations derived from FEM, achieving strong enforcement of physics and boundary conditions with improved solution fidelity [12].

In the context of magnetized micropolar fluid flows, the integration of artificial intelligence-based solvers such as Neural FEM is still at an early stage [13]. The present work represents one of the first applications of a neural finite element framework to solve magneto-micropolar boundary value systems with comparison to classical solvers such as `bvp4c`. This thesis explores the performance, accuracy, and physical insights offered by Neural FEM solutions in comparison with traditional numerical techniques, focusing on key parameters like Reynolds number, Prandtl number, skin-friction coefficient, Nusselt number, and micromagnetorotation effects [14]. Moreover, boundary layer flows involving micropolar fluids have received substantial attention in recent years because they offer an effective framework for modeling complex fluids with inherent microstructural effects, including polymeric suspensions, liquid crystals, and biological fluids. Unlike Newtonian fluids, micropolar fluids account for the microrotation of fluid particles and the associated angular momentum effects, leading to more accurate descriptions of real-world phenomena. The inclusion of microrotation introduces additional governing equations, thereby increasing the mathematical complexity of the system. Consequently, the accurate prediction of velocity, microrotation, and temperature fields requires robust numerical methods capable of effectively handling the strong coupling and nonlinear characteristics of the governing system [14–16]. Moreover, the application of an external magnetic field further modifies the flow characteristics by introducing magnetohydrodynamic (MHD) effects, thereby increasing the complexity of the governing dynamics. These phenomena are encountered in a wide range of engineering applications, including electromagnetic pumping, nuclear cooling technologies, metallurgical processes, and plasma physics. The coupling between the magnetic field and the electrically conducting fluid gives rise to Lorentz forces, which exert a significant influence on the flow dynamics and heat transfer characteristics. Accurately modeling such interactions requires solving highly nonlinear and coupled systems of differential equations, making them suitable for advanced computational techniques such as Neural FEM and physics-informed learning frameworks [11, 13, 17]. An important stage in the numerical modeling of boundary layer flows is the application of suitable transformations that reduce the governing partial differential equations to a system of ordinary differential equations, thereby facilitating their numerical solution. This is achieved using the application of similarity transformations. This approach reduces computational complexity and allows for efficient numerical treatment of the problem. Nevertheless, the resulting nonlinear ordinary differential system often presents considerable numerical difficulties owing to stiffness, sensitivity to initial guesses, and the presence of multiple interacting parameters. Traditional computational approaches, including shooting-based algorithms and collocation solvers such as `bvp4c`, are commonly applied to boundary value problems in fluid mechanics. Nevertheless, their efficiency and robustness can deteriorate when the governing equations become highly nonlinear or exhibit strong inter-variable coupling. To overcome these limitations, neural network–based methodologies have gained attention as a promising alternative. These approaches are particularly attractive because they do not rely on mesh-based discretization and are capable of learning complex nonlinear mappings directly from the governing system [5, 18, 19]. Moreover, recent advancements in computational intelligence have highlighted the importance of adaptive and data-driven solution strategies for nonlinear boundary value problems. Techniques such as deep learning-based surrogate modeling, residual minimization, and variational neural networks have demonstrated significant potential in reducing computational cost while maintaining acceptable accuracy levels. In particular, the integration of automatic differentiation within neural network frameworks allows for precise evaluation of derivatives, which is essential for enforcing governing equations in strong or weak forms. This capability makes neural approaches especially attractive for high-dimensional and multiphysics problems where traditional discretization methods may become computationally prohibitive. Despite these advantages, challenges such as training instability, hyperparameter sensitivity, and convergence reliability persist, necessitating further investigation and hybridization with classical numerical schemes to ensure robustness and efficiency [5, 6, 20].

Physics-Informed Neural Networks (PINNs) have recently gained prominence as an effective computational framework for solving nonlinear partial differential equations by incorporating the underlying physical laws into the network training process through the loss function [21]. Furthermore, developments in physics-informed machine learning have highlighted their capability to accurately and flexibly model complex multiphysics phenomena while avoiding the need for conventional mesh-based discretization techniques [22]. Artificial neural networks have also been successfully applied to approximate solutions of boundary value problems, providing an alternative to classical numerical techniques. Hybrid approaches combining neural networks with variational principles have shown promising results in enhancing solution stability and convergence for PDE-based problems. Furthermore, studies on the generalization and error behavior of neural network solvers highlight both their potential and limitations in comparison with conventional numerical methods such as FEM [13]. The application of the (FEM) to magneto-micropolar fluid flows has been extensively investigated in recent studies. In particular, FEM provides a robust framework for solving the highly coupled nonlinear differential equations arising in micropolar fluid dynamics [23]. The flexibility of FEM in handling complex boundary conditions and nonlinearities makes it especially suitable for modeling magneto-micropolar boundary layer problems. It has been demonstrated that FEM-based approaches yield accurate and stable solutions when compared with classical numerical techniques, particularly for higher values of governing physical parameters [24]. In addition to standard FEM formulations, the use of computational tools such as FreeFEM++ has further enhanced the capability of numerical simulations in fluid dynamics. FreeFEM++ allows efficient implementation of variational formulations and Galerkin-based methods for solving partial differential equations. Studies have shown that micropolar fluid flows under the influence of magnetic fields can be effectively simulated using FreeFEM++, providing detailed insights into velocity, microrotation, and temperature distributions [25]. Moreover, the incorporation of micromagnetorotation (MMR) effects has introduced a new dimension in the study of micropolar fluids. The MMR parameter significantly influences the rotational behavior of fluid particles and alters the structure of the boundary layer. The numerical analysis demonstrates that higher values of the micromagnetorotation parameter produce significant variations in the velocity and microrotation distributions, highlighting the importance of including such effects in realistic fluid flow models. Galerkin-type numerical schemes have also been employed to enhance the accuracy and stability of solutions for nonlinear systems [26]. The Galerkin–Petrov method, in particular, provides an efficient approach for discretizing time-dependent and steady-state problems. This method has been successfully applied to nonlinear differential equations arising in fluid flow problems, demonstrating improved convergence characteristics and reduced computational errors. Overall, the contributions of FEM-based studies in magneto-micropolar fluid dynamics establish a strong foundation for further advancements in computational modeling. These classical numerical approaches not only provide reliable benchmark solutions but also serve as a basis for the development of modern hybrid techniques such as Neural FEM. By integrating data-driven methods with established FEM frameworks, it becomes possible to achieve enhanced computational efficiency and improved solution accuracy for complex multiphysics problems [24]. Moreover, studies on boundary layer flows of micropolar fluids have revealed that thermophysical properties and external forcing mechanisms significantly affect the flow dynamics and overall transport behavior. In particular, studies focusing on heat transfer enhancement in micropolar and nanofluid systems reveal that variations in thermal conductivity, viscous dissipation, and magnetic parameters significantly influence temperature and velocity distributions. The FEM has proven to be highly effective in capturing these coupled effects, providing accurate numerical predictions for engineering applications involving thermal management and energy systems [27]. In addition, numerical studies on nonlinear fluid flow problems using advanced computational techniques have highlighted the importance of stability and convergence in obtaining reliable solutions. The implementation of iterative solvers within FEM frameworks has shown improved performance in handling stiff and highly nonlinear systems. Such approaches enable efficient resolution of complex governing equations arising in magnetohydrodynamic and micropolar flow problems, thereby offering a strong computational foundation for extending classical methods toward modern data-driven frameworks such as Neural FEM [28].

Finally, the motivation of the present work lies in bridging the gap between traditional numerical methods and emerging data-driven approaches to solving complex fluid flow problems. By integrating neural network architectures with finite element principles, the Neural FEM framework aims to provide improved solution accuracy, reduced dependency on mesh generation, and enhanced capability to handle nonlinear multiphysics systems [29]. The comparative analysis carried out in this study not only evaluates the effectiveness of Neural FEM against established numerical solvers but also highlights its potential for future applications in computational fluid dynamics and heat transfer. This work contributes to the growing body of research focused on leveraging artificial intelligence to solve challenging engineering problems and opens new avenues for the development of hybrid computational methodologies [11, 30].

1.1 Thesis Contribution

This section outlines the key contributions made in this thesis.

i. This thesis presents the development and implementation of a Neural FEM to solve the nonlinear boundary value problem governing magnetized micropolar fluid flow and heat transfer. The application of similarity transformations converts the governing system into a set of ordinary differential equations discussed in existing literature. The solution strategy is fundamentally different, employing a neural-based finite element framework instead of classical numerical solvers.

ii. A systematic comparison is carried out between the proposed Neural FEM solutions and the benchmark numerical results obtained using the MATLAB solver bvp4c. The comparison is presented through detailed tabulated results for key physical quantities, demonstrating the accuracy, reliability, and consistency of the Neural FEM approach for solving coupled nonlinear boundary value systems.

iii. The study highlights the effectiveness of Neural FEM as an alternative computational tool for complex fluid flow problems by analyzing important physical parameters such as Reynolds number, Prandtl number, skin-friction coefficient, Nusselt number, and micromagnetorotation. The results indicate that Neural FEM can successfully capture the underlying physics of magneto-micropolar flows while offering a flexible framework that bridges classical finite element formulations and modern neural network techniques.

1.2 Thesis Layout

This thesis is organized into the following chapters:

i. In **Chapter 2** , the mathematical formulation of the problem is developed for micromagnetorotational fluid flow with heat transfer based on micropolar fluid dynamics. The governing mathematical model is established using the fundamental conservation principles of mass, momentum, angular momentum, and energy. The effects of magnetization and electromagnetic forces are also incorporated into the model.

ii. In **Chapter 3**, a detailed description of the FEM and GFEM is provided. The numerical procedure is explained through illustrative one-dimensional and two-dimensional example problems. Moreover, this chapter presents a concise theoretical overview of the FEM and neural networks, followed by a clear formulation of their mathematical connection. An illustrative example is included to demonstrate how the weak formulation of the governing equations can be integrated with a neural network approximation, thereby establishing the fundamental relationship underlying the Neural FEM framework.

iii. In **Chapter 4**, the numerical investigation of magnetized micropolar fluid flow coupled with heat transfer is presented and discussed. At the outset, the governing dimensional equations are reduced to a system of ordinary differential equations through the application of appropriate similarity transformations. The transformed boundary value problem is subsequently solved using the Neural Finite Element Method. A comparative study is carried out between the proposed Neural FEM results and the classical numerical solutions obtained using the MATLAB solver `bvp4c`. The influence of key physical parameters, including the Reynolds number, Prandtl number, skin-friction coefficient, Nusselt number, and micromagnetorotation effects, is systematically analyzed and discussed. The computed results are illustrated through both graphs and tables.

iv. In **Chapter 5**, the main findings of the thesis are highlighted with the key conclusions drawn from the present investigation. Possible directions for future research are also outlined.

Chapter 2

Mathematical Model of Micromagnetorotation with Heat Transfer in Micropolar Fluid Theory

2.1 Physical Model

The physical model considered in this study consists of a steady, two-dimensional, incompressible flow of an electrically conducting micropolar fluid over a stretching surface in the presence of an externally applied magnetic field. The fluid is assumed to exhibit both translational and microrotational motion, which characterizes the behavior of micropolar fluids. The stretching surface generates a boundary layer flow, while heat transfer takes place simultaneously within the fluid domain. A Cartesian coordinate framework is adopted in which the x-axis is taken parallel to the direction of the free-stream flow, while the y-axis is considered normal to the surface. A uniform magnetic field is applied normal to the stretching surface, which induces magnetohydrodynamic effects and influences both the momentum and thermal transport processes. The magnetization of the fluid and its interaction with the microrotation of fluid particles give rise to the MMR effect, which significantly affects the flow behavior.

The governing equations include the continuity equation, momentum equation, angular momentum equation, magnetic induction equation, magnetization equation, and energy equation. These equations describe the coupled interaction between fluid velocity, microrotation, induced magnetic field, magnetization, and temperature distribution. Appropriate similarity transformations are employed to convert the governing partial differential equations into a system of nonlinear ordinary differential equations, making them suitable for numerical solution using the NFEM.

The vector form of the governing equations is as follows: [31]

$$\nabla \cdot \mathbf{U} = 0, \tag{2.1}$$

$$\nabla \cdot \mathbf{H} = 0, \tag{2.2}$$

$$\begin{aligned} \rho\left(\frac{\partial \mathbf{U}}{\partial t} + (\mathbf{U}\cdot\nabla)\mathbf{U}\right) = & -\nabla p + \tilde{\eta}\nabla^2\mathbf{U} + 2\eta_1\nabla\times(\mathbf{W}-\boldsymbol{\omega}) \\ & + (\nabla\times\mathbf{H})\times\mathbf{B} + \mathbf{M}\times(\nabla\times\mathbf{H}) + (\mathbf{M}\cdot\nabla)\mathbf{H}, \end{aligned} \tag{2.3}$$

$$\rho\left(\frac{\partial \mathbf{H}}{\partial t} + (\mathbf{U}\cdot\nabla)\mathbf{H}\right) = (\mathbf{H}\cdot\nabla)\mathbf{U} + \tilde{\eta}\nabla^2\mathbf{H}, \tag{2.4}$$

$$l\left(\frac{\partial \mathbf{W}}{\partial t} + (\mathbf{U}\cdot\nabla)\mathbf{W}\right) = \gamma\nabla^2\mathbf{W} + \mathbf{M}\times\mathbf{H} + 4\eta_1(\boldsymbol{\omega}-\mathbf{W}), \tag{2.5}$$

$$\mathbf{B} = \mu_0(\mathbf{H}+\mathbf{M}), \tag{2.6}$$

$$\mathbf{M} = M_0\left(\frac{\mathbf{H}}{H} - \tau\,\mathbf{W}\times\boldsymbol{\epsilon}\right), \tag{2.7}$$

$$\mathbf{J} = \nabla\times\mathbf{H}, \tag{2.8}$$

$$\mathbf{J} = \sigma\left(\mathbf{E} + \mathbf{U}\times\mathbf{B}\right). \tag{2.9}$$

In this context, the variables are defined as follows:

- ρ denotes the fluid density,

- p represents the pressure,
- $\mathbf{J}$ is the current density,
- l is the rotational inertia,
- μ_0 is the magnetic permeability,
- σ is the electrical conductivity,
- $\mathbf{B}$ refers to the magnetic induction vector,
- $\tilde{\eta}$ is the shear viscosity,
- η_1 is the vortex viscosity,
- γ is the angular viscosity,
- $\mathbf{M} \times \mathbf{H}$ describes the micromagnetorotation (MMR) effect, which accounts for how magnetization influences microrotation.

2.2 Governing Equations in the Operator Form

This section derives the operator form of the governing equations from their vector form. While the vector form captures the underlying physical principles in a compact, abstract notation, the operator form recasts these relations explicitly in terms of the system's physical variables and parameters. This explicit structure is generally more convenient for subsequent analytical or numerical treatment.

2.2.1 Continuity Equation

The continuity equation is given as follows.

$$\nabla \cdot \mathbf{U} = 0. \tag{2.10}$$

In two-dimension, its compoenet form can be calculated as

$$\left(\frac{\partial}{\partial x}, \frac{\partial}{\partial y}, 0 \right) \cdot (u, v, 0) = 0. \tag{2.11}$$

$$\Rightarrow \frac{\partial u}{\partial x} + \frac{\partial v}{\partial y} = 0. \tag{2.12}$$

The conservation of magnetization is given by

$$\nabla \cdot \mathbf{H} = 0. \tag{2.13}$$

In two-dimensional component form it becomes

$$\frac{\partial H_1}{\partial x} + \frac{\partial H_2}{\partial y} = 0. \tag{2.14}$$

2.2.2 Momentum Equation

The convective part of the momentum equation is given by

$$\mathbf{U} \cdot \nabla \mathbf{U} = (u, v, 0) \cdot \left(\frac{\partial}{\partial x}, \frac{\partial}{\partial y}, \right) (u, v, 0), \tag{2.15}$$

$$= u \frac{\partial}{\partial x}(u, v, 0) + v \frac{\partial}{\partial y}(u, v, 0). \tag{2.16}$$

$$\Rightarrow \mathbf{U} \cdot \nabla \mathbf{U} = \left(u\frac{\partial u}{\partial x} + v\frac{\partial u}{\partial y},\ u\frac{\partial v}{\partial x} + v\frac{\partial v}{\partial y},\ 0 \right). \tag{2.17}$$

The Laplacian of the velocity is calculated as

$$\nabla^2 \mathbf{U} = \left(\frac{\partial^2 u}{\partial x^2} + \frac{\partial^2 u}{\partial y^2},\ \frac{\partial^2 v}{\partial x^2} + \frac{\partial^2 v}{\partial y^2},\ 0 \right). \tag{2.18}$$

2.2.3 Curl Terms

The curl of the difference of rotational velocities is given by

$$2\eta_1 \nabla \times (\mathbf{W} - \mathbf{w}) = 2\eta_1 (\nabla \times \mathbf{W}) - 2\eta_1 (\nabla \times \mathbf{w}), \tag{2.19}$$

$$= 2\eta_1(\nabla \times \mathbf{W}) - 2\eta_1 \left(\nabla \times \left(\nabla \times \frac{\mathbf{U}}{2}\right)\right). \tag{2.20}$$

Curl of $\mathbf{W} = (0, 0, N)$: The curl of W is calculated as follows.

$$\nabla \times \mathbf{W} = \begin{vmatrix} \hat{i} & \hat{j} & \hat{k} \\ \frac{\partial}{\partial x} & \frac{\partial}{\partial y} & 0 \\ 0 & 0 & N \end{vmatrix} = \left(\frac{\partial N}{\partial y}, -\frac{\partial N}{\partial x}, 0\right). \tag{2.21}$$

Curl of $\mathbf{U}$- velocity is calculated as

$$\nabla \times \mathbf{U} = \begin{vmatrix} \hat{i} & \hat{j} & \hat{k} \\ \frac{\partial}{\partial x} & \frac{\partial}{\partial y} & 0 \\ u & v & 0 \end{vmatrix} = \left(0, 0, \frac{\partial v}{\partial x} - \frac{\partial u}{\partial y}\right). \tag{2.22}$$

Curl of Curl of $\mathbf{U}$ is calculated as

$$\nabla \times (\nabla \times \mathbf{U}) = \begin{vmatrix} \hat{i} & \hat{j} & \hat{k} \\ \frac{\partial}{\partial x} & \frac{\partial}{\partial y} & 0 \\ 0 & 0 & \frac{\partial v}{\partial x} - \frac{\partial u}{\partial y} \end{vmatrix}, \tag{2.23}$$

$$= \left(\frac{\partial^2 v}{\partial y \partial x} - \frac{\partial^2 u}{\partial y^2}, \; -\left(\frac{\partial^2 v}{\partial x^2} - \frac{\partial^2 u}{\partial x \partial y}\right), \; 0\right). \tag{2.24}$$

The magnetic flux term

$$\mathbf{J} \times \mathbf{B} = \sigma(\mathbf{E} + \mathbf{U} \times \mathbf{B}) \times \mathbf{B} \approx \sigma(\mathbf{U} \times \mathbf{B}) \times \mathbf{B}, \tag{2.25}$$

is calculated as follows.

Evaluation of $\mathbf{U} \times \mathbf{B}$:

$$\mathbf{U} \times \mathbf{B} = \mu_0 \begin{vmatrix} \hat{i} & \hat{j} & \hat{k} \\ u & v & 0 \\ H_1 + M_0 & H_2 - \tau M_0 N & 0 \end{vmatrix}. \tag{2.26}$$

The cross product $\mathbf{U} \times \mathbf{B}$ represents the interaction between the fluid velocity field and the applied magnetic field. The determinant form given in Eq. (2.26) is used to evaluate this vector product in component form.

Here, $\mathbf{U} = (u, v, 0)$ denotes the velocity field, while $\mathbf{B} = (H_1 + M_0,\ H_2 - \tau M_0 N,\ 0)$ represents the effective magnetic field incorporating the magnetization effects.

This term plays a crucial role in magnetohydrodynamics as it contributes to the Lorentz force when further crossed with the magnetic field, which directly influences the momentum transport within the fluid.

$$\mathbf{U} \times \mathbf{B} = \mu_0 \left(uH_2 - u\tau M_0 N - vH_1 - vM_0 \right) \hat{k}. \tag{2.27}$$

Evaluation of $(\mathbf{U} \times \mathbf{B}) \times \mathbf{B}$:

$$(\mathbf{U} \times \mathbf{B}) \times \mathbf{B} = \mu_0 \begin{vmatrix} \hat{i} & \hat{j} & \hat{k} \\ 0 & 0 & uH_2 - u\tau M_0 N - vH_1 - vM_0 \\ H_1 + M_0 & H_2 - \tau M_0 N & 0 \end{vmatrix}. \tag{2.28}$$

The expression obtained in Eq. (2.28) represents the Lorentz force term $(\mathbf{U} \times \mathbf{B}) \times \mathbf{B}$, which is generated by the interaction of the fluid motion with the imposed magnetic field. In addition to this electromagnetic body force, the contribution of magnetization must also be taken into account. This effect is incorporated through the term $(\mathbf{M}\cdot\nabla)\mathbf{H}$, it denotes the force generated by spatial changes in magnetic field intensity acting on the magnetized fluid. The magnetization force plays a significant role in micromagnetorotation fluid flows, particularly when the magnetic properties of the fluid interact with non-uniform magnetic fields. Unlike the Lorentz force, which arises from the interaction between the induced current and the magnetic field, the magnetization force is associated with the alignment of magnetic particles and their response to spatial variations in magnetic field strength. The detailed evaluation of the term $(\mathbf{M}\cdot\nabla)\mathbf{H}$ is presented below.

$$
\begin{aligned}
(\mathbf{U}\times\mathbf{B})\times\mathbf{B} = \mu_0\Bigg[\Big(& - uH_2^2 + 2u\tau M_0NH_2 - u\tau^2M_0^2N^2 \\
&+ vH_1H_2 + vM_0H_2 - v\tau M_0NH_1 - v\tau M_0^2N\Big)\hat{\imath} \\
&+ \Big(uH_1H_2 - u\tau M_0NH_1 + uM_0H_2 - u\tau M_0^2N \\
&- vH_1^2 - 2vM_0H_1 - vM_0^2\Big)\hat{\jmath}\Bigg],
\end{aligned}
\tag{2.29}
$$

and

$$
\begin{aligned}
(\mathbf{M}\cdot\nabla)\mathbf{H} &= (M_x, M_y, 0)\cdot\nabla(H_1, H_2, 0) \\
&= M_x\frac{\partial(H_1,H_2,0)}{\partial x} + M_y\frac{\partial(H_1,H_2,0)}{\partial y} \\
&= \Bigg(M_x\frac{\partial H_1}{\partial x} + M_y\frac{\partial H_1}{\partial y}, \\
&\qquad M_x\frac{\partial H_2}{\partial x} + M_y\frac{\partial H_2}{\partial y}, 0\Bigg).
\end{aligned}
\tag{2.30}
$$

The above expression decomposes the term $(\mathbf{M}\cdot\nabla)\mathbf{H}$ into its Cartesian components. It shows that the magnetic body force depends not only on the magnetic field intensity but also on its spatial variations. These component-wise relations are used in the subsequent formulation of the momentum equations to describe the coupling between the magnetic field and the micropolar fluid motion.

2.2.4 The Cross Product $\mathbf{M} \times (\nabla \times \mathbf{H})$

As,

$$\nabla \times \mathbf{H} = \begin{vmatrix} \hat{i} & \hat{j} & \hat{k} \\ \frac{\partial}{\partial x} & \frac{\partial}{\partial y} & 0 \\ H_1 & H_2 & 0 \end{vmatrix}.$$

$$\Rightarrow \nabla \times \mathbf{H} = (0)\,\hat{i} - (0)\,\hat{j} + \left(\frac{\partial H_2}{\partial x} - \frac{\partial H_1}{\partial y}\right)\hat{k}.$$

$$\mathbf{M} \times (\nabla \times \mathbf{H}) = \begin{vmatrix} \hat{i} & \hat{j} & \hat{k} \\ M_0 \frac{(H_1+\tau H_2 N)}{H_1} & M_0 \frac{(H_2-\tau H_1 N)}{H_2} & 0 \\ 0 & 0 & \left(\frac{\partial H_2}{\partial x} - \frac{\partial H_1}{\partial y}\right) \end{vmatrix} \tag{2.31}$$

$$= \left[M_0 \frac{(H_2 - \tau H_1 N)}{H_2}\left(\frac{\partial H_2}{\partial x} - \frac{\partial H_1}{\partial y}\right)\right]\hat{i}$$

$$- \left[M_0 \frac{(H_1 + \tau H_2 N)}{H_1}\left(\frac{\partial H_2}{\partial x} - \frac{\partial H_1}{\partial y}\right)\right]\hat{j} + 0\hat{k}.$$

The term $\nabla \times \mathbf{H}$ represents the curl of the magnetic field, which describes the rotational behavior of the magnetic field intensity in the flow domain. From the above evaluation, it is observed that only the k-component is non-zero due to the two-dimensional nature of the flow.

The cross product $\mathbf{M} \times (\nabla \times \mathbf{H})$ therefore gives rise to force components in the x- and y-directions, as shown in Eq. (2.31). This term represents the coupling between magnetization and the spatial gradients of the magnetic field, which significantly affects momentum transport and microrotational behavior within the fluid.

2.2.5 Final Form of the Momentum Equation

Now, substituting all the expressions (2.17)–(2.31) into equation (2.3), we obtain:

$$
\begin{aligned}
\rho\left(\frac{du}{dt},\frac{dv}{dt},0\right)+\left(u\frac{\partial u}{\partial x}+v\frac{\partial u}{\partial y},\ u\frac{\partial v}{\partial x}+v\frac{\partial v}{\partial y},\ 0\right) = &-\left(\frac{\partial p}{\partial x},\frac{\partial p}{\partial y},0\right)\\
&+\mu\Bigg(\frac{\partial^2 u}{\partial x^2}+\frac{\partial^2 u}{\partial y^2},\\
&\quad\frac{\partial^2 v}{\partial x^2}+\frac{\partial^2 v}{\partial y^2},\ 0\Bigg)\\
&+2\zeta_1\left(\frac{\partial N}{\partial y}-\frac{\partial N}{\partial x},0,0\right)\\
&-\zeta_1\Bigg(\frac{\partial^2 v}{\partial y\partial x}-\frac{\partial^2 u}{\partial y^2},\\
&\quad-\frac{\partial^2 v}{\partial x^2}-\frac{\partial^2 u}{\partial x\partial y},\ 0\Bigg)\\
&+\sigma\mu_0\left(\mathcal{F}_x,\mathcal{F}_y,0\right).
\end{aligned}
\tag{2.32}
$$

The above equation represents the complete momentum equation governing the magneto-micropolar fluid flow. It incorporates the effects of fluid inertia, viscous diffusion, microrotation, and electromagnetic body forces. The interaction between the magnetic field and the magnetized fluid is accounted for through the Lorentz force and magnetization terms, thereby describing the coupled influence of hydrodynamic and magnetic phenomena on the flow behavior.

To facilitate further analysis, the vector momentum equation is resolved into its scalar components along the x- and y-directions. Under the boundary-layer assumptions, the resulting system reduces to a set of coupled nonlinear partial differential equations subject to appropriate surface and far-field boundary conditions. The corresponding x-momentum equation is obtained from the first component of the vector equation and is given by:

$$
\begin{aligned}
\frac{\partial u}{\partial t} + u\frac{\partial u}{\partial x} + v\frac{\partial u}{\partial y} = -\frac{1}{\rho}\frac{\partial p}{\partial x} + \frac{\mu}{\rho}\left(\frac{\partial^2 u}{\partial x^2}\right. \\
&+ \frac{\partial^2 u}{\partial y^2} \qquad + \qquad \frac{2\zeta_1}{\rho}\frac{\partial N}{\partial y} \\
&+ \frac{\zeta_1}{\rho}\left(\frac{\partial^2 u}{\partial y^2} - \frac{\partial^2 v}{\partial x \partial y}\right) \\
&- \frac{\sigma\mu_0}{\rho}\left(uH_2^2\right) \\
&+ \frac{\sigma\mu_0}{\rho}\left(2u\tau M_0 N H_2 - u\tau^2 M_0^2 N^2\right) \\
&+ \frac{\sigma\mu_0}{\rho}\left(+vH_1H_2 + vM_0H_2\right) \\
&- \frac{\sigma\mu_0}{\rho}\left(v\tau M_0 N H_1 + v\tau M_0^2 N\right) \\
&+ \frac{M_0}{\rho}\left(\frac{H_1 + \tau H_2 N}{H_1}\frac{\partial H_1}{\partial x}\right) \\
&+ \frac{M_0}{\rho}\left(+\frac{H_2 - \tau H_1 N}{H_2}\frac{\partial H_1}{\partial y}\right).
\end{aligned} \tag{2.33}
$$

Equation (2.33) represents the dimensional momentum equation in the x-direction for the present magneto-micropolar fluid flow. The equation includes the effects of pressure gradient, viscous diffusion, and microrotation through the spin viscosity terms. In addition, the electromagnetic body force arising from the Lorentz force, $(\mathbf{U} \times \mathbf{B}) \times \mathbf{B}$, and the magnetic body force associated with the magnetization term, $(\mathbf{M} \cdot \nabla)\mathbf{H}$, are explicitly incorporated. Consequently, the equation describes the coupled interaction between the fluid flow, microrotation, and magnetic field, which governs the momentum transport in the presence of micromagnetorotation effects. titlesec

2.2.5.1 The Magnetic Induction Equation

To calculate the magnetic induction equation we proceed as follows.

$$
\begin{aligned}
\mathbf{U}\cdot\nabla\mathbf{H} &= (u,v,0)\cdot\left(\frac{\partial}{\partial x},\frac{\partial}{\partial y},0\right)(H_1,H_2,0)\\
&= \left(u\frac{\partial}{\partial x}+v\frac{\partial}{\partial y}\right)(H_1,H_2,0)\\
&= u\frac{\partial}{\partial x}(H_1,H_2,0)+v\frac{\partial}{\partial y}(H_1,H_2,0)\\
&= \left(u\frac{\partial H_1}{\partial x},u\frac{\partial H_2}{\partial x},0\right)+\left(v\frac{\partial H_1}{\partial y},v\frac{\partial H_2}{\partial y},0\right)\\
&= \left(u\frac{\partial H_1}{\partial x}+v\frac{\partial H_1}{\partial y},\ u\frac{\partial H_2}{\partial x}+v\frac{\partial H_2}{\partial y},\ 0\right).
\end{aligned}
\tag{2.34}
$$

$$
\begin{aligned}
\mathbf{H}\cdot\nabla\mathbf{U} &= (H_1,H_2,0)\cdot\left(\frac{\partial}{\partial x},\frac{\partial}{\partial y},0\right)(u,v,0)\\
&= \left(H_1\frac{\partial}{\partial x},H_2\frac{\partial}{\partial y},0\right)(u,v,0)\\
&= H_1\frac{\partial}{\partial x}(u,v,0)+H_2\frac{\partial}{\partial y}(u,v,0)\\
&= \left(H_1\frac{\partial u}{\partial x},H_1\frac{\partial v}{\partial x},0\right)+\left(H_2\frac{\partial u}{\partial y},H_2\frac{\partial v}{\partial y},0\right)\\
&= \left(H_1\frac{\partial u}{\partial x}+H_2\frac{\partial u}{\partial y},\ H_1\frac{\partial v}{\partial x}+H_2\frac{\partial v}{\partial y},\ 0\right).
\end{aligned}
\tag{2.35}
$$

$$
\begin{aligned}
\nabla^2\mathbf{H} &= \left(\frac{\partial}{\partial x},\frac{\partial}{\partial y},0\right)\cdot\left(\frac{\partial}{\partial x},\frac{\partial}{\partial y},0\right)(H_1,H_2,0)\\
&= \left(\frac{\partial^2}{\partial x^2}+\frac{\partial^2}{\partial y^2}\right)(H_1,H_2,0)\\
&= \left(\frac{\partial^2 H_1}{\partial x^2},\frac{\partial^2 H_2}{\partial x^2},0\right)+\left(\frac{\partial^2 H_1}{\partial y^2},\frac{\partial^2 H_2}{\partial y^2},0\right)\\
&= \left(\frac{\partial^2 H_1}{\partial x^2}+\frac{\partial^2 H_1}{\partial y^2},\ \frac{\partial^2 H_2}{\partial x^2}+\frac{\partial^2 H_2}{\partial y^2},\ 0\right).
\end{aligned}
\tag{2.36}
$$

Now, we put all expressions (2.34)–(2.36) into equation (2.4) to get the following.

$$
\begin{aligned}
\rho\left[\left(\frac{dH_1}{dt},\frac{dH_2}{dt},0\right)\right]+\Bigg[\bigg(u\frac{\partial H_1}{\partial x}+v\frac{\partial H_1}{\partial y},\ u\frac{\partial H_2}{\partial x}+v\frac{\partial H_2}{\partial y},\ 0\bigg)\Bigg]&\\
-\left(H_1\frac{\partial u}{\partial x}+H_2\frac{\partial u}{\partial y},\ H_1\frac{\partial v}{\partial x}+H_2\frac{\partial v}{\partial y},\ 0\right)&\\
=\mu_0\left(\frac{\partial^2 H_1}{\partial x^2}+\frac{\partial^2 H_1}{\partial y^2},\ \frac{\partial^2 H_2}{\partial x^2}+\frac{\partial^2 H_2}{\partial y^2},\ 0\right)&\\
\Rightarrow \frac{dH_1}{dt}+\left(u\frac{\partial H_1}{\partial x}+v\frac{\partial H_1}{\partial y}\right)-\left(H_1\frac{\partial u}{\partial x}+H_2\frac{\partial u}{\partial y}\right)&\\
=\frac{\mu_0}{\rho}\left(\frac{\partial^2 H_1}{\partial x^2}+\frac{\partial^2 H_1}{\partial y^2}\right)&\\
\Rightarrow u\frac{\partial H_1}{\partial x}+v\frac{\partial H_1}{\partial y}=H_1\frac{\partial v}{\partial x}+H_2\frac{\partial u}{\partial y}+k\left(\frac{\partial^2 H_1}{\partial y^2}\right).&
\end{aligned}
\tag{2.37}
$$

Similarly, we can transform the governing equation (2.5) from vector form into the operator form.

Chapter 3

Fundamentals of the Finite Element Method

Although the Finite Element Method (FEM) and the Finite Volume Method (FVM) are built on different discretization philosophies, they rest on several shared conceptual foundations. A key first step in FEM is the discretization of the computational domain into simple geometric elements: triangles or quadrilaterals are commonly used for two-dimensional problems, while tetrahedra or hexahedra serve the same purpose in three dimensions. Once this discretization is complete, the governing equations are multiplied by appropriate weight functions prior to being integrated over the domain.

Continuity of the solution across neighboring elements is a central requirement in FEM. In its basic form, this is achieved by approximating the solution within each element using linear shape functions constructed from the values at the element's nodes. Substituting this approximation into the weighted-residual form of the governing conservation equations, and setting the derivative of the resulting integral with respect to each nodal value to zero, leads directly to a discrete algebraic system. This chapter demonstrates the procedure using one- and two-dimensional Poisson equations as representative test cases.

3.1 Finite Element Approaches

The FEM is a widely adopted computational technique for approximating solutions of boundary value problems encountered in engineering and applied sciences. Its fundamental idea is based on dividing the entire problem domain into a collection of smaller, simpler regions known as finite elements. Within each element, the unknown variables are represented using appropriate interpolation or shape functions.

In the formulation process, the governing differential equations are not solved directly in their strong form. Instead, they are reformulated into an equivalent weak or variational form by applying weighted residual techniques or variational principles. The resulting system of algebraic equations is then assembled from individual element contributions and solved to obtain the numerical approximation of the solution field. Due to its flexibility in handling complex geometries, boundary conditions, and coupled physical phenomena, FEM has become one of the most widely used numerical methods in fluid dynamics and heat transfer [3, 4].

FEM models can be developed using a range of methodological approaches, such as:

- Galerkin Finite Element Method
- Direct Method
- Variational Method
- Method of Weighted Residual
- Neural Finite Element Method

3.1.1 Direct Method

The direct formulation is one of the basic approaches used in the development of the Finite Element Method (FEM). It begins by partitioning the physical domain into a set of smaller regions referred to as finite elements. Within each element, the dependent variable is approximated using suitable interpolation or shape functions. For an element containing n nodes, the approximate representation of the solution can be expressed as follows:

$$u(x) \approx \sum_{i=1}^{n} N_i(x) u_i, \tag{3.1}$$

where $N_i(x)$ denote the interpolation (shape) functions and u_i correspond to the nodal quantities of the unknown parameter.

Using the governing physical principles, such as equilibrium or conservation laws, the element equations are derived and expressed in matrix form as

$$[K^e]\{u^e\} = \{F^e\}, \tag{3.2}$$

Here, $[K^e]$ is the element stiffness matrix, $\{u^e\}$ represents the vector of unknown nodal values for the element, and $\{F^e\}$ is the element load vector. The global system of equations is then formed by assembling the individual element equations across the entire domain.

$$[K]\{U\} = \{F\}, \tag{3.3}$$

Here, $[K]$ represents the global stiffness matrix, $\{U\}$ the vector of global nodal unknowns, and $\{F\}$ the global force vector. Applying the appropriate boundary conditions to this system allows the unknown nodal values to be determined by solving the resulting set of algebraic equations.

3.1.2 Variational Method

The variational method provides a systematic framework for developing the finite element formulation by converting the governing differential equation into an equivalent variational or weak form. Consider a general second-order differential equation defined over a domain :

$$-\frac{d}{dx}\left(k\frac{du}{dx}\right) = f(x), \quad x \in \Omega, \tag{3.4}$$

along with the corresponding boundary conditions.

Within the variational formulation, the governing problem is expressed in terms of a functional J(u), here, the function that minimizes this functional represents the exact solution of the differential equation.. A typical functional can be written as

$$J(u) = \int_{\Omega} \left[\frac{1}{2}k\left(\frac{du}{dx}\right)^2 - f(x)u\right] dx. \tag{3.5}$$

The approximate solution is obtained by requiring that the first variation of the functional vanishes, i.e.,

$$\delta J(u) = 0. \tag{3.6}$$

The unknown variable within each finite element is represented using an approximation based on interpolation shape functions.

$$u(x) \approx \sum_{i=1}^{n} N_i(x)u_i, \tag{3.7}$$

where $N_i(x)$ denote the interpolation (shape) functions and u_i correspond to the nodal quantities of the unknown parameter. Substituting this approximation into the variational formulation and performing the necessary integrations leads to the element matrix equation

$$[K^e]\{u^e\} = \{F^e\}. \tag{3.8}$$

Finally, assembling all element equations yields the global system

$$[K]\{U\} = \{F\}, \tag{3.9}$$

which can be solved after imposing the boundary conditions.

3.1.3 Method of Weighted Residual

Among the available formulations, the method of weighted residuals is particularly well-suited for solving problems governed by differential equations. A brief description of the weighted residual approach is presented below.

Suppose a boundary value problem is described by the differential equation stated below:

$$\mathcal{L}u = f(x), \tag{3.10}$$

where $f(x)$ represents a prescribed source term, $u(x)$ is the unknown dependent variable to be determined, and $\mathcal{L}$ is a differential operator acting on u. To approximate the exact solution, a trial function $\tilde{u}(x)$ is introduced that satisfies the specified boundary conditions but does not, in general, exactly satisfy the governing differential equation. Consequently, substituting $\tilde{u}(x)$ into the equation produces a nonzero residual

$$R(\tilde{u}) = \mathcal{L}\tilde{u} - f \neq 0. \tag{3.11}$$

Let the trial solution be assumed in the following form:

$$\tilde{u}(x) = \sum_{i=1}^{N} u_i \phi_i(x), \tag{3.12}$$

Here, $\phi_i(x)$ denote the basis functions. As the space spanned by these basis functions is finite-dimensional, the residual $R(\tilde{u})$ generally fails to vanish everywhere in the domain. In order to minimize this residual, as expressed in Eq. (3.11), the following condition is imposed:

$$\int_\Omega w(x) R(\tilde{u})\, d\Omega = 0, \tag{3.13}$$

for a set of weight functions $w(x)$ constructed as:

$$w(x) = \sum_{i=1}^{N} w_i \psi_i(x), \tag{3.14}$$

Here, $\psi_i(x)$ denote known basis functions, while w_i are the unknown scalar coefficients to be found. The resulting system of equations takes the form:

$$[A]\mathbf{u} = \mathbf{F}, \tag{3.15}$$

where $[A]$ is the system stiffness matrix, $\mathbf{u}$ contains the unknown nodal coefficients that are to be found, and $\mathbf{F}$ denotes the corresponding source (or load) vector of the system.

Example:

To demonstrate the implementation of the weighted residual method, a one-dimensional boundary value problem is considered in this illustration.

To proceed, we focus on solving the following differential equation:

$$\frac{d^2u}{dx^2} - u = -x, \quad \text{for } 0 < x < 1, \quad u(0) = u(1) = 0. \tag{3.16}$$

Choose a trial function that satisfies the specified boundary conditions.

$$\tilde{u}(x) = ax(1-x). \tag{3.17}$$

Substituting the expression from Eq. (3.17) into the governing differential equation in Eq. (3.16) gives the residual, which reduces to

$$R(x) = \frac{d^2\tilde{u}}{dx^2} - \tilde{u} + x = -2a - ax(1-x) + x. \tag{3.18}$$

Expanding and simplifying Eq. (3.18) gives

$$R(x) = -2a - ax + ax^2 + x. \tag{3.19}$$

Using the Galerkin method, the weight function is chosen as

$$w(x) = \frac{d\tilde{u}}{da} = x(1-x). \tag{3.20}$$

The weighted residual condition in Eq. (3.19) becomes

$$\int_0^1 (x - x^2)(-2a - ax + ax^2 + x)\, dx = 0. \tag{3.21}$$

Solving the above integral yields $a \approx 0.2267$.Using Eq. (3.17), this can be written as

$$\tilde{u}(x) = 0.2267x(1-x). \tag{3.22}$$

This represents the solution to the boundary value problem considered in Eq. (3.16).

3.1.4 Illustrative Example of Weighted Residual Method

To demonstrate how the weighted residual method works in practice, the following one-dimensional boundary value problem is considered:

$$\frac{d^2u}{dx^2} + 1 = 0, \quad 0 \leq x \leq 1 \tag{3.23}$$

subject to the boundary conditions

$$u(0) = 0, \quad u(1) = 0. \tag{3.24}$$

The approximate solution $\tilde{u}(x)$ is taken as a trial function satisfying the essential boundary conditions, expressed as:

$$\tilde{u}(x) = a_1 x(1-x), \tag{3.25}$$

where a_1 is an unknown coefficient to be determined.

Substituting the approximate solution into the governing equation yields the corresponding residual equation:

$$R(x) = \frac{d^2\tilde{u}}{dx^2} + 1. \tag{3.26}$$

Evaluating the derivatives,

$$\frac{d^2\tilde{u}}{dx^2} = -2a_1, \tag{3.27}$$

so that the residual becomes

$$R(x) = -2a_1 + 1. \tag{3.28}$$

The Galerkin method requires that the residual be orthogonal to the chosen weighting function, which is chosen as the same as the trial function:

$$\int_0^1 R(x)\, x(1-x)\, dx = 0. \tag{3.29}$$

Substituting $R(x)$,

$$\int_0^1 (-2a_1 + 1)\, x(1-x)\, dx = 0. \tag{3.30}$$

Evaluating the integral,

$$(-2a_1 + 1) \int_0^1 (x - x^2)\, dx = 0. \tag{3.31}$$

$$\Rightarrow (-2a_1 + 1) \left[\frac{x^2}{2} - \frac{x^3}{3} \right]_0^1 = 0. \tag{3.32}$$

$$\Rightarrow (-2a_1 + 1) \left(\frac{1}{2} - \frac{1}{3} \right) = 0. \tag{3.33}$$

$$\Rightarrow (-2a_1 + 1) \left(\frac{1}{6} \right) = 0. \tag{3.34}$$

Thus,

$$-2a_1 + 1 = 0 \quad \Rightarrow \quad a_1 = \frac{1}{2}. \tag{3.35}$$

Therefore, the approximate solution is obtained as

$$\tilde{u}(x) = \frac{1}{2}x(1-x). \tag{3.36}$$

As shown in this example, an approximate analytical solution to a boundary value problem can be obtained through the weighted residual method, specifically the Galerkin approach, without requiring explicit discretization of the domain.

3.2 Galerkin Finite Element Method

Among the various techniques available, the Galerkin method is one of the most widely used for constructing finite element formulations of differential equations. Its fundamental concept involves representing the unknown solution through a combination of basis (shape) functions and ensuring that the governing equations are satisfied in an averaged or integral sense.

The main procedural steps of the GFEM are outlined below.

Step 1: Governing differential equation

Let a general differential equation be defined over a domain Ω, expressed as:

$$\mathcal{L}(u) = f \quad \text{in } \Omega, \tag{3.37}$$

Here, $\mathcal{L}$ represents a differential operator, u is the unknown function to be solved for, and f is a given source term.

Step 2: Approximate solution

An approximation to the unknown function is constructed using a finite combination of basis functions.

$$u(x) \approx u_h(x) = \sum_{i=1}^{n} N_i(x) u_i, \tag{3.38}$$

where $N_i(x)$ denote the interpolation (shape) functions and u_i correspond to the nodal quantities of the unknown parameter.

Step 3: Residual formulation

Substituting the approximate solution into the governing equation produces a residual

$$R(x) = \mathcal{L}(u_h) - f. \tag{3.39}$$

Step 4: Galerkin condition

The Galerkin method requires the residual to be orthogonal to the weighting functions, which are taken to be identical to the shape functions. This choice yields

$$\int_{\Omega} N_j(x) R(x)\, d\Omega = 0, \qquad j = 1, 2, \ldots, n. \tag{3.40}$$

Step 5: Weak Formulation

Substituting the residual expression into the above equation leads to the weak (integral) form of the governing equation.

Step 6: Element equations

The domain is divided into finite elements, and the above formulation is applied to each element to obtain the element matrix equation

$$[K^e]\{u^e\} = \{F^e\}. \tag{3.41}$$

Step 7: Assembly and solution

Finally, the element equations are assembled to form the global system

$$[K]\{U\} = \{F\}, \tag{3.42}$$

which can be solved after applying the appropriate boundary conditions.

3.2.1 Example: (Two-Dimensional Poisson Equation)

Consider the two-dimensional Poisson equation defined on a domain Ω as

$$-\nabla^2 u = f(x, y), \qquad (x, y) \in \Omega \tag{3.43}$$

subject to the boundary condition

$$u = 0, \qquad (x, y) \in \partial\Omega \tag{3.44}$$

where ∇^2 denotes the Laplacian operator

$$\nabla^2 u = \frac{\partial^2 u}{\partial x^2} + \frac{\partial^2 u}{\partial y^2}. \tag{3.45}$$

Weak Formulation

The weak form is obtained by multiplying the governing equation by a weighting function v and integrating the result over the domain Ω, which gives

$$\int_\Omega v(-\nabla^2 u)\, d\Omega = \int_\Omega vf\, d\Omega. \tag{3.46}$$

Using Green's theorem and integration by parts, the weak form becomes

$$\int_\Omega \nabla v \cdot \nabla u\, d\Omega = \int_\Omega vf\, d\Omega. \tag{3.47}$$

Finite Element Approximation

The approximate solution is expressed using shape functions

$$u_h(x, y) = \sum_{i=1}^{n} N_i(x, y) u_i, \tag{3.48}$$

where $N_i(x, y)$ are the interpolation (shape) functions and u_i are the nodal unknowns.

In the Galerkin method, the weighting functions are chosen as

$$v = N_j(x, y). \tag{3.49}$$

Substituting the approximation into the weak form yields

$$\int_\Omega \nabla N_j \cdot \nabla \left(\sum_{i=1}^{n} N_i u_i \right) d\Omega = \int_\Omega N_j f \, d\Omega. \tag{3.50}$$

Rearranging the terms gives the finite element equation

$$\sum_{i=1}^{n} \left[\int_\Omega \nabla N_j \cdot \nabla N_i \, d\Omega \right] u_i = \int_\Omega N_j f \, d\Omega. \tag{3.51}$$

Matrix form

The system in Eq.(3.51) can be written in matrix form as

$$[K]\{U\} = \{F\}, \tag{3.52}$$

where

$$K_{ij} = \int_\Omega \nabla N_i \cdot \nabla N_j \, d\Omega, \tag{3.53}$$

is the stiffness matrix and

$$F_i = \int_\Omega N_i f \, d\Omega, \tag{3.54}$$

is the load vector. After assembling all element matrices and applying boundary conditions, the resulting algebraic system is solved to obtain the approximate nodal solution.

3.2.2 Galerkin Finite Element Formulation for 2D Poisson Equation

Consider the two-dimensional Poisson equation defined over a domain Ω with boundary Γ:

$$-\nabla^2 u = f \quad \text{in } \Omega, \tag{3.55}$$

subject to the Dirichlet boundary condition

$$u = 0 \quad \text{on } \Gamma. \tag{3.56}$$

The governing equation can be written in expanded form as

$$-\left(\frac{\partial^2 u}{\partial x^2} + \frac{\partial^2 u}{\partial y^2}\right) = f. \tag{3.57}$$

To obtain the weak (variational) form, we multiply the governing equation by a weighting function w and integrate over the domain Ω:

$$\int_\Omega w(-\nabla^2 u) \, d\Omega = \int_\Omega w f \, d\Omega. \tag{3.58}$$

Applying Green's theorem and integration by parts, we obtain

$$\int_\Omega \nabla w \cdot \nabla u \, d\Omega - \int_\Gamma w \frac{\partial u}{\partial n} \, d\Gamma = \int_\Omega w f \, d\Omega. \tag{3.59}$$

For Dirichlet boundary conditions, the weighting function w vanishes on Γ, and hence the boundary term disappears. Therefore, the weak form reduces to

$$\int_\Omega \nabla w \cdot \nabla u \, d\Omega = \int_\Omega w f \, d\Omega. \tag{3.60}$$

In the Galerkin finite element method, both the approximate solution u_h and the weighting (test) function w are represented using the same set of shape functions N_i, leading to

$$u_h = \sum_{j=1}^{n} N_j u_j, \quad w = N_i, \tag{3.61}$$

where u_j denotes the nodal unknowns and n represents the total number of nodes in the element or domain.

Substituting into the weak form, we obtain

$$\int_\Omega \nabla N_i \cdot \nabla \left(\sum_{j=1}^{n} N_j u_j \right) d\Omega = \int_\Omega N_i f \, d\Omega. \tag{3.62}$$

This can be written as

$$\sum_{j=1}^{n} \left(\int_\Omega \nabla N_i \cdot \nabla N_j \, d\Omega \right) u_j = \int_\Omega N_i f \, d\Omega. \tag{3.63}$$

Thus, the system of algebraic equations can be expressed in matrix form as

$$\mathbf{K}\mathbf{u} = \mathbf{F}, \tag{3.64}$$

where the stiffness matrix $\mathbf{K}$ and force vector $\mathbf{F}$ are respectively defined as

$$K_{ij} = \int_\Omega \nabla N_i \cdot \nabla N_j \, d\Omega, \tag{3.65}$$

and

$$F_i = \int_\Omega N_i f \, d\Omega. \tag{3.66}$$

The computational domain Ω is divided into a finite number of elements, and the required integrals are evaluated locally over each element. The global algebraic system is then constructed by assembling the contributions from all individual elements. After imposing the prescribed boundary conditions, the resulting system of linear equations is solved to determine the nodal values of the approximate solution u_h.

This framework constitutes the foundation of the Galerkin finite element method for the solution of two-dimensional Poisson-type problems and can be readily extended to more complex partial differential equations arising in fluid flow and heat transfer applications.

3.3 Connection with Neural FEM

By discretizing the governing partial differential equations, the Galerkin finite element formulation described above yields an efficient system of algebraic equations, offering a robust numerical strategy for solving such problems. However, its implementation typically depends on mesh generation and the explicit construction of shape functions over individual elements. In contrast, the Neural Finite Element Method (Neural FEM) extends this framework by replacing or enhancing conventional interpolation functions with neural network-based approximators. Neural networks (NNs) are computational frameworks whose design draws inspiration from the structure and function of biological neural systems. An artificial neural network (ANN) consists of interconnected processing units, known as neurons, organized in layers. These layers process input information and generate corresponding outputs through weighted connections and nonlinear activation functions.

Neural networks exhibit strong function approximation capabilities and have been demonstrated to effectively represent complex nonlinear mappings with high accuracy.Recent years have seen growing use of artificial neural networks (ANNs) as a means of numerically solving differential equations. This is typically achieved within an optimization-based framework, where the residuals of both the governing equations and their boundary conditions are minimized. Their mesh-free formulation and capability to address high-dimensional problems make them attractive alternatives to conventional numerical solvers [5, 8]. The Neural Finite Element Method (Neural FEM) integrates the rigorous mathematical structure of the FEM with the approximation capabilities of artificial neural networks. In this hybrid formulation, neural networks are used as trial (basis) functions within the finite element framework, thereby replacing or enhancing the traditional polynomial-based shape functions.

By embedding neural networks into the FEM formulation, Neural FEM retains the variational structure, boundary condition enforcement, and physical consistency of FEM, while benefiting from the adaptive learning and generalization capabilities of neural networks. This integration allows for improved accuracy in handling nonlinearities, steep gradients, and singular behaviors often encountered in fluid flow and heat transfer problems.

Neural FEM is particularly well-suited for complex boundary value problems where traditional methods may face convergence difficulties, offering a robust and flexible framework that bridges physics-based modeling and data-driven learning [6, 8, 9].

In Neural FEM, the approximate solution $u_h(x, y)$ is represented using a neural network, such that

$$u_h(x, y) \approx \mathcal{N}(x, y; \boldsymbol{\theta}), \tag{3.67}$$

where $\mathcal{N}$ denotes a neural network parameterized by weights and biases $\boldsymbol{\theta}$. Unlike conventional FEM, where the solution is constructed using predefined polynomial basis functions, the neural network serves as a global approximator.

The Galerkin weak form can then be incorporated into a loss function by minimizing the residual of the variational formulation. Specifically, the loss function can be defined as

$$\mathcal{L}(\boldsymbol{\theta}) = \sum_{i=1}^{N} \left| \int_\Omega \nabla N_i \cdot \nabla \mathcal{N}(x, y; \boldsymbol{\theta}) \, d\Omega - \int_\Omega N_i f \, d\Omega \right|^2, \tag{3.68}$$

where N_i are test (weighting) functions, and N represents the number of sampling or collocation points.

Alternatively, a strong-form residual minimization can also be employed, leading to a physics-informed loss of the form

$$\mathcal{L}(\boldsymbol{\theta}) = \frac{1}{N_r} \sum_{k=1}^{N_r} \left| -\nabla^2 \mathcal{N}(x_k, y_k; \boldsymbol{\theta}) - f(x_k, y_k) \right|^2, \tag{3.69}$$

augmented with boundary condition penalties.

Thus, Neural FEM combines the variational foundation of the Galerkin method with the function approximation power of neural networks. This hybridization eliminates the need for explicit mesh generation while retaining the physical consistency of the governing equations. Moreover, the use of automatic differentiation enables accurate computation of spatial derivatives required in the formulation. As a result, Neural FEM provides a flexible and efficient framework for solving complex, nonlinear, and higher order partial differential equations encountered in fluid dynamics and heat transfer.

3.3.1 Illustrative Example Linking FEM and Neural Networks

The following one-dimensional boundary value problem is defined over the domain $\Omega = (0, 1)$:

$$-\frac{d^2 u}{dx^2} = f(x), \quad 0 < x < 1, \tag{3.70}$$

subject to the boundary conditions

$$u(0) = 0, \quad u(1) = 0. \tag{3.71}$$

Within the finite element framework, the weak form of the problem is obtained by multiplying the governing equation by a test function $v(x)$, followed by integration over the domain:

$$\int_0^1 \frac{du}{dx}\frac{dv}{dx}\,dx = \int_0^1 f(x)v(x)\,dx. \tag{3.72}$$

The approximate solution $u_h(x)$ is expressed as a linear combination of polynomial shape functions $N_i(x)$:

$$u_h(x) = \sum_{i=1}^{n} N_i(x)\,u_i, \tag{3.73}$$

where u_i represent the nodal parameters. Substituting this approximation into the weak form yields a system of algebraic equations in terms of the unknown nodal quantities.

By contrast, in a neural network-based approach, the approximate solution is represented instead by a neural network $\mathcal{N}(x;\theta)$, parameterized by trainable weights θ:

$$u_h(x) \approx \mathcal{N}(x;\theta). \tag{3.74}$$

The network parameters are obtained by minimizing a loss function constructed from the residual of the governing equation together with the boundary conditions:

$$\mathcal{L}(\theta) = \int_0^1 \left(\frac{d^2\mathcal{N}}{dx^2} + f(x)\right)^2 dx + |\mathcal{N}(0)|^2 + |\mathcal{N}(1)|^2. \tag{3.75}$$

In the Neural Finite Element Method, the neural network replaces the classical polynomial shape functions while retaining the variational structure of FEM. The trial solution is written as

$$u_h(x) = \sum_{e=1}^{n_e} \mathcal{N}_e(x;\theta_e), \tag{3.76}$$

where $\mathcal{N}_e(x;\theta_e)$ represents a neural network defined locally over each finite element.

The weak form is preserved, but the neural network parameters are optimized instead of nodal values. This formulation combines the physical consistency and boundary condition enforcement of FEM with the powerful approximation capability of neural networks. This example demonstrates that classical FEM and neural networks differ mainly in the choice of approximation functions. While FEM relies on fixed polynomial basis functions, Neural FEM employs adaptive neural network-based basis functions within the same variational framework. Consequently, the Neural Finite Element Method (Neural FEM) can be regarded as a natural extension of the classical finite element framework, where neural network-based approximators enhance or replace traditional interpolation functions while preserving the underlying variational structure.

Chapter 4

Micromagnetorotation Boundary Layer Flow and Heat Transfer Model

This chapter focuses on developing and numerically analyzing a mathematical model for magnetized micropolar fluid flow with heat transfer in a porous medium, accounting for the effects of thermal radiation. The analysis begins with the formulation of a coupled system of nonlinear partial differential equations representing conservation of mass, linear and angular momentum, and energy.

Using appropriate similarity transformations, these governing equations are converted from their dimensional form into a dimensionless coupled system of ordinary differential equations. The weak (variational) form of this system is then derived, providing the basis for the numerical solution scheme. To solve the resulting boundary value problem, the Neural Finite Element Method is employed — a technique that merges the variational structure of the classical Galerkin finite element approach with the function-approximation capability of artificial neural networks. This hybrid strategy yields stable and accurate results even under strong nonlinear behavior, radiative heating, and resistance imposed by the porous medium.

Finally, the chapter examines in detail how various physical parameters influence the velocity, microrotation, and temperature distributions.

4.1 Geometry of the Problem

In this model, a steady, two-dimensional, incompressible boundary layer flow of an electrically conducting micropolar fluid is considered over a semi-infinite flat plate situated in a porous medium. The stretching surface is oriented along the x-axis and is stretched with a prescribed velocity, while the y-axis is taken normal to the surface. The coordinate system, along with the formation of the velocity, thermal, and microrotation boundary layers, is shown in Figure 4.1.

A constant transverse magnetic field of magnitude H_0 acts normal to the stretching surface. Assuming a sufficiently small magnetic Reynolds number, the induced magnetic field is neglected relative to the applied field. Darcy's resistance model is used to capture the impedance exerted by the porous medium on the fluid motion. In addition, thermal radiation effects are incorporated to account for radiative heat transfer within the boundary layer region.

The fluid is assumed to possess micropolar characteristics, allowing the microelements to undergo independent rotational motion described by the microrotation component. At the stretching surface ($y = 0$), appropriate boundary conditions are imposed for the velocity, temperature, and microrotation fields, while far away from the surface ($y \to \infty$), the fluid is assumed to be quiescent with ambient temperature T_∞ and vanishing microrotation. Under these assumptions, the flow and heat transfer processes are governed by a coupled system of momentum, angular momentum, and energy equations.

4.2 Governing Equations in Vector-Tensor Form

Along with the boundary layer approximations (as illustrated in Figure 4.1), the governing system of Eqs. (1)–(9) can be simplified and expressed in the following component form. This reduction allows for a more tractable formulation of the problem while retaining the essential physical characteristics of the flow, making it suitable for further analytical and numerical investigations. The governing equations are as follows: [31]

$$u\frac{\partial u}{\partial x} + v\frac{\partial u}{\partial y} = (\frac{\mu + k}{\rho})\frac{\partial^2 u}{\partial y^2} - \frac{\sigma}{\rho}\mu_0 H_0^2 u + \frac{k}{\rho}\frac{\partial \phi}{\partial y} + \frac{1}{\rho}M_0 \bar{H} H_1 \frac{\partial H_1}{\partial x}, \tag{4.1}$$

$$u\frac{\partial H_1}{\partial x} + v\frac{\partial H_1}{\partial y} = H_1\frac{\partial u}{\partial x} + H_2\frac{\partial u}{\partial y} + \eta\frac{\partial^2 H_1}{\partial y^2}, \tag{4.2}$$

$$u\frac{\partial \phi}{\partial x} + v\frac{\partial \phi}{\partial y} = \frac{\gamma^*}{\rho_j}\frac{\partial^2 \phi}{\partial y^2} - \frac{k}{\rho_j}\phi^2 + \frac{\partial u}{\partial y} - M_0 H_0 \tau \bar{H}\phi, \tag{4.3}$$

$$u\frac{\partial T}{\partial x} + v\frac{\partial T}{\partial y} = \frac{\kappa}{\rho C_p}\frac{\partial^2 T}{\partial y^2} + \frac{k}{\rho C_p}\left(\frac{\partial u}{\partial y}\right)^2 + \frac{4k}{\rho C_p}\phi\left(\frac{\partial u}{\partial y}\right)^2 + \frac{\tau M_0 H_0^2 \bar{H}}{\rho C_p}\phi^2. \tag{4.4}$$

The governing system in Eqs. (4.1)-(4.4) are solved under the prescribed boundary conditions [31]

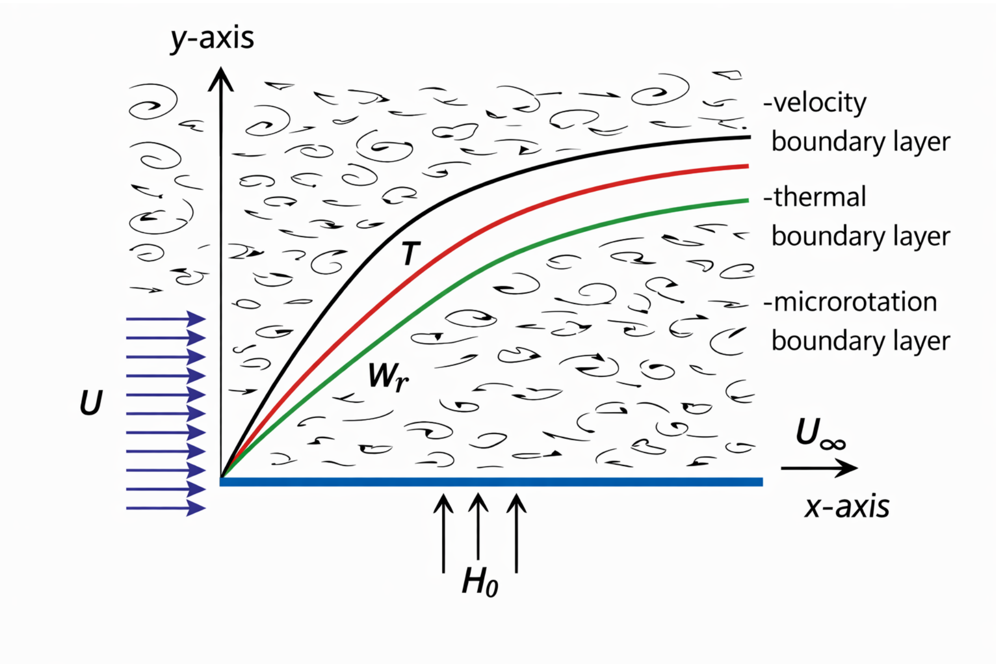

FIGURE 4.1: Schematic illustration of the boundary layer flow of a micropolar fluid over a porous surface

$$\begin{cases} \quad H_1 = 0, \quad u = U_\infty, \quad H_2 = H_0\sqrt{\dfrac{\nu x}{U_\infty}}, \quad v = 0, \\ \Omega = -\Omega_0 \dfrac{\partial u}{\partial y}, \quad T = T_w, \qquad \text{at } y = 0, \\ u \to 0, \quad \phi \to 0, \quad H_1 \to 0, \quad T \to T_\infty, \qquad \text{as } y \to \infty. \end{cases} \tag{4.5}$$

The boundary conditions prescribed in Eq. (4.5) are selected on the basis of their

physical relevance and applicability to a wide range of practical situations. In particular, the present study examines the flow of a micropolar fluid over a magnetized stretching sheet under these conditions, motivated by their importance in several industrial and engineering processes. Such configurations commonly arise in polymer processing, especially during the manufacture of plastic films, as well as in coating and printing technologies.

Moreover, these boundary conditions are useful for modeling the spreading of thin liquid films over solid surfaces and for analyzing fiber behavior in textile manufacturing [31]. In these applications, understanding the flow structure, understanding shear stress behavior and boundary layer development is essential.

4.3 Conversion to ODE Form

To facilitate the analysis, the following similarity transformations are introduced.

$$\phi \equiv \begin{cases} T = T_\infty + (T_w - T_\infty)\,\theta(\xi), \\ \psi = U_\infty P(\xi)\sqrt{\dfrac{\nu x}{U_\infty}} \\ \xi = y\sqrt{\dfrac{U_\infty}{\nu x}}, \\ u = \dfrac{\partial \psi}{\partial y}, \qquad v = -\dfrac{\partial \psi}{\partial x}, \\ \Omega = U_\infty\sqrt{\dfrac{U_\infty}{\nu x}}\,R(\xi), \\ H_1 = H_0 x\,Q'(\xi), \qquad H_2 = -H_0\sqrt{\dfrac{\nu x}{U_\infty}}\,Q(\xi). \end{cases} \tag{4.6}$$

By applying the similarity transformations given in Eq.(4.6) to the governing equations (4.1)–(4.5), the original system of partial differential equations is transformed into a set of coupled non-linear boundary value problems as follows:

4.3.1 Transformation of Momentum Equation into ODE Form

The dimensional momentum equation is given by

$$u\frac{\partial u}{\partial x} + v\frac{\partial u}{\partial y} = \frac{\mu + k}{\rho}\frac{\partial^2 u}{\partial y^2} - \frac{\sigma}{\rho}\mu_0 H_\infty^2\, u + \frac{k}{\rho}\frac{\partial \phi}{\partial y} + \frac{1}{\rho}M_0 \bar{H}\bar{H}_1\frac{\partial H_1}{\partial x}. \tag{4.1}$$

The partial derivatives of ξ with respect to x and y are:

$$\frac{\partial \xi}{\partial y} = \sqrt{\frac{U_\infty}{\nu x}}, \qquad \frac{\partial \xi}{\partial x} = -\frac{\xi}{2x}. \tag{4.7}$$

The streamwise velocity derivatives follow as:

$$\frac{\partial u}{\partial x} = U_\infty P''(\xi)\cdot\left(-\frac{\xi}{2x}\right) = -\frac{U_\infty\,\xi}{2x}\,P''(\xi), \tag{4.8}$$

$$\frac{\partial u}{\partial y} = U_\infty P''(\xi)\cdot\sqrt{\frac{U_\infty}{\nu x}} = \frac{U_\infty^{3/2}}{(\nu x)^{1/2}}\,P''(\xi), \tag{4.9}$$

$$\frac{\partial^2 u}{\partial y^2} = \frac{U_\infty^{3/2}}{(\nu x)^{1/2}}\,P'''(\xi)\cdot\sqrt{\frac{U_\infty}{\nu x}} = \frac{U_\infty^2}{\nu x}\,P'''(\xi). \tag{4.10}$$

Substituting (4.8), (4.9) and (4.10) into the left-hand side of equation (4.1):

$$\begin{aligned} u\frac{\partial u}{\partial x} + v\frac{\partial u}{\partial y} &= U_\infty P'\cdot\left(-\frac{U_\infty\,\xi}{2x}\right)P'' + \frac{1}{2}\sqrt{\frac{\nu U_\infty}{x}}\big[\xi P' - P\big]\cdot\frac{U_\infty^{3/2}}{(\nu x)^{1/2}}\,P'' \\ &= -\frac{U_\infty^2}{2x}\,\xi P'P'' + \frac{U_\infty^2}{2x}\big[\xi P' - P\big]P'' \\ &= \frac{U_\infty^2}{2x}\left[-\xi P'P'' + \xi P'P'' - PP''\right] = -\frac{U_\infty^2}{2x}\,PP''. \end{aligned} \tag{4.11}$$

The $\xi P'P''$ terms cancel exactly. For the right-hand side, the viscous-micropolar term transforms as:

$$\frac{\mu + k}{\rho}\frac{\partial^2 u}{\partial y^2} = \left(1 + \frac{k}{\mu}\right)\frac{U_\infty^2}{\nu x}\,P''' = (1+K)\,\frac{U_\infty^2}{\nu x}\,P''', \tag{4.12}$$

where $K = k/\mu$ is the micropolar coupling parameter. The magnetic drag term gives:

$$-\frac{\sigma\,\mu_0 H_\infty^2}{\rho}\,u = -\frac{\sigma\,\mu_0 H_\infty^2}{\rho}\,U_\infty P' = -M^2\frac{U_\infty^2}{\nu x}\,P', \tag{4.13}$$

where the Hartmann parameter is defined as $M^2 = \sigma\,\mu_0 H_\infty^2\,\nu x/(\rho\,U_\infty)$. The microrotation coupling term, using $\Omega = U_\infty\sqrt{U_\infty/(\nu x)}\,R(\xi)$, gives:

$$\frac{k}{\mu}\frac{\partial\phi}{\partial y} = \frac{k}{\mu}\cdot\frac{U_\infty^2}{\nu x}\,R' = K\,\frac{U_\infty^2}{\nu x}\,R'. \tag{4.14}$$

For the magnetic pressure term, using $H_1 = H_0\,x\,Q'(\xi)$ with $\bar{H} \approx H_\infty$ and $\bar{H}_1 \approx H_0\,Q$:

$$\frac{\partial H_1}{\partial x} = H_0\left(Q' - \frac{\xi}{2}Q''\right), \tag{4.15}$$

$$\frac{1}{\rho}M_0\bar{H}\bar{H}_1\frac{\partial H_1}{\partial x} = \frac{M_0\,\mu_0\,H_0^2\,H_\infty}{\rho}\,Q\,Q' = \lambda\,\frac{U_\infty^2}{\nu x}\,Q\,Q', \tag{4.16}$$

where $\lambda = M_0\,\mu_0\,H_0^2\,\nu/(\rho\,U_\infty^2)$ is the dimensionless magnetization parameter. Collecting all terms and dividing through by the common factor $U_\infty^2/(\nu x)$:

$$-\frac{1}{2}\,PP'' = (1+K)\,P''' - M^2P' + K\,R' + \lambda\,QQ'. \tag{4.17}$$

Rearranging into standard form yields the ODE:

$$\boxed{(1+K)\,P''' + \frac{1}{2}\,PP'' - M^2P' + K\,R' + \lambda\,QQ' = 0.} \tag{4.18}$$

The boundary conditions (4.5) transform under (4.6) as follows. At the wall $\xi = 0$:

$$u = U_\infty \;\Rightarrow\; P'(0) = 1, \qquad v = 0 \;\Rightarrow\; P(0) = 0, \qquad Q'(0) = 0, \qquad Q(0) = -1. \tag{4.19}$$

As $\xi \to \infty$:

$$u \to 0 \;\Rightarrow\; P'(\infty) = 0, \qquad Q'(\infty) = 0. \tag{4.20}$$

The condition $P'(\infty) = 0$ indicates that the fluid velocity approaches the quiescent ambient state away from the wall. Similarly, $Q'(\infty) = 0$ ensures that the microrotational effects diminish in the free-stream region, satisfying the physical requirements of the problem.

4.3.2 Transformation of Magnetic Field Transport Equation into ODE Form

The magnetic field transport equation is:

$$u\frac{\partial H_1}{\partial x} + v\frac{\partial H_1}{\partial y} = H_1\frac{\partial u}{\partial x} + H_2\frac{\partial u}{\partial y} + \eta\frac{\partial^2 H_1}{\partial y^2} \tag{4.2}$$

where η is the magnetic diffusivity. Using the similarity transformations (4.6), the derivatives of $H_1 = H_0\, x\, Q'(\xi)$ are computed as:

$$\frac{\partial H_1}{\partial x} = H_0\, Q'(\xi) + H_0\, x\, Q''(\xi) \cdot \left(-\frac{\xi}{2x}\right) = H_0\left(Q' - \frac{\xi}{2}Q''\right), \tag{4.21}$$

$$\frac{\partial H_1}{\partial y} = H_0\, x\, Q''(\xi) \cdot \sqrt{\frac{U_\infty}{\nu x}} = H_0\sqrt{\frac{U_\infty x}{\nu}}\, Q''(\xi), \tag{4.22}$$

$$\frac{\partial^2 H_1}{\partial y^2} = H_0\sqrt{\frac{U_\infty x}{\nu}}\, Q'''(\xi) \cdot \sqrt{\frac{U_\infty}{\nu x}} = H_0\, \frac{U_\infty}{\nu}\, Q'''(\xi). \tag{4.23}$$

Substituting into the left side of equation (4.2):

$$\begin{aligned}
u\frac{\partial H_1}{\partial x} + v\frac{\partial H_1}{\partial y} &= U_\infty F' \cdot H_0\left(Q' - \frac{\xi}{2}Q''\right) + \frac{1}{2}\sqrt{\frac{\nu U_\infty}{x}}\left[\xi F' - F\right] \cdot H_0\sqrt{\frac{U_\infty x}{\nu}}\,Q'' \\
&= U_\infty H_0\left(F'Q' - \frac{\xi}{2}F'Q''\right) + \frac{U_\infty H_0}{2}\left[\xi F' - F\right]Q'' \\
&= U_\infty H_0\left[F'Q' - \frac{\xi}{2}F'Q'' + \frac{\xi}{2}F'Q'' - \frac{1}{2}FQ''\right] \\
&= U_\infty H_0\left[F'Q' - \frac{1}{2}FQ''\right]. \qquad (4.24)
\end{aligned}$$

The $\xi F'Q''$ terms cancel exactly. For the right-hand side, recalling $\partial u/\partial x = -U_\infty \xi F''/(2x)$ and $\partial u/\partial y = U_\infty^{3/2}/(\nu x)^{1/2}\, F''$, the three terms evaluate as:

$$H_1\frac{\partial u}{\partial x} = H_0\, x\, Q' \cdot \left(-\frac{U_\infty\, \xi}{2x}\right) F'' = -\frac{U_\infty H_0\, \xi}{2}\, Q'F'', \qquad (4.25)$$

$$H_2\frac{\partial u}{\partial y} = \left(-H_0\sqrt{\frac{\nu x}{U_\infty}}\, Q\right) \cdot \frac{U_\infty^{3/2}}{(\nu x)^{1/2}}\, F'' = -U_\infty H_0\, QF'', \qquad (4.26)$$

$$\eta\,\frac{\partial^2 H_1}{\partial y^2} = \eta \cdot H_0\,\frac{U_\infty}{\nu}\, Q''' = \frac{1}{P_m}\, U_\infty H_0\, Q''', \qquad (4.27)$$

where the magnetic Prandtl number is $P_m = \nu/\eta$. Collecting all right-hand side terms:

$$\text{RHS} = U_\infty H_0\left[-\frac{\xi}{2}\, F''Q' - F''Q + \frac{1}{P_m}\, Q'''\right]. \qquad (4.28)$$

Equating left- and right-hand sides and dividing through by the common factor $U_\infty H_0$:

$$F'Q' - \frac{1}{2}FQ'' = -\frac{\xi}{2}\, F''Q' - F''Q + \frac{1}{P_m}\, Q'''. \qquad (4.29)$$

Rearranging into standard form yields the ODE:

$$\boxed{\frac{1}{P_m}\, Q''' + \frac{1}{2}FQ'' - F'Q' - F''Q - \frac{\xi}{2}\, F''Q' = 0.} \qquad (4.30)$$

The boundary conditions (4.5) transform under (4.6) as follows. At the wall $\xi = 0$:

$$H_1 = 0 \;\Rightarrow\; Q'(0) = 0, \qquad H_2 = H_0\sqrt{\frac{\nu x}{U_\infty}} \;\Rightarrow\; Q(0) = -1. \tag{4.31}$$

As $\xi \to \infty$:

$$H_1 \to 0 \;\Rightarrow\; Q'(\infty) = 0. \tag{4.32}$$

4.3.3 Transformation of Microrotation Transport Equation into ODE form

The microrotation transport equation is:

$$u\frac{\partial\phi}{\partial x} + v\frac{\partial\phi}{\partial y} = \frac{\gamma^*}{\rho_j}\frac{\partial^2\phi}{\partial y^2} - \frac{k}{\rho_j}\phi + \frac{k}{\rho_j}\frac{\partial u}{\partial y} - M_0H_0\,\tau\,\bar{H}\,\phi \tag{4.3}$$

where γ^* is the spin-gradient viscosity, ρ_j is the microinertia density, k is the vortex viscosity, τ is the magnetic torque coefficient, and $\bar{H} \approx H_\infty$. Under the similarity transformations (4.6), the microrotation is:

$$\phi \equiv \Omega = U_\infty\sqrt{\frac{U_\infty}{\nu x}}\,R(\xi) = \frac{U_\infty^{3/2}}{(\nu x)^{1/2}}\,R(\xi). \tag{4.33}$$

Defining the prefactor $\mathcal{A}(x) = U_\infty^{3/2}(\nu x)^{-1/2}$, the derivatives of ϕ are:

$$\frac{\partial\phi}{\partial x} = -\frac{\mathcal{A}}{2x}\big[R + \xi R'\big] = -\frac{U_\infty^{3/2}}{2x(\nu x)^{1/2}}\big[R + \xi R'\big], \tag{4.34}$$

$$\frac{\partial\phi}{\partial y} = \mathcal{A}\,R'(\xi)\cdot\sqrt{\frac{U_\infty}{\nu x}} = \frac{U_\infty^2}{\nu x}\,R'(\xi), \tag{4.35}$$

$$\frac{\partial^2\phi}{\partial y^2} = \frac{U_\infty^2}{\nu x}\,R''(\xi)\cdot\sqrt{\frac{U_\infty}{\nu x}} = \frac{U_\infty^{5/2}}{(\nu x)^{3/2}}\,R''(\xi). \tag{4.36}$$

Substituting into the left-hand side of equation (4.3):

$$\begin{aligned}
u\frac{\partial\phi}{\partial x}+v\frac{\partial\phi}{\partial y} &= U_\infty F'\cdot\left(-\frac{U_\infty^{3/2}}{2x(\nu x)^{1/2}}\right)\left[R+\xi R'\right]+\frac{1}{2}\sqrt{\frac{\nu U_\infty}{x}}\left[\xi F'-F\right]\cdot\frac{U_\infty^2}{\nu x}R' \\
&= -\frac{U_\infty^{5/2}}{2x(\nu x)^{1/2}}\left[F'R+\xi F'R'\right]+\frac{U_\infty^{5/2}}{2x(\nu x)^{1/2}}\left[\xi F'R'-FR'\right] \\
&= \frac{U_\infty^{5/2}}{2x(\nu x)^{1/2}}\left[-F'R-\xi F'R'+\xi F'R'-FR'\right] \\
&= -\frac{U_\infty^{5/2}}{2x(\nu x)^{1/2}}\left[F'R+FR'\right]=-\frac{U_\infty^{5/2}}{2x(\nu x)^{1/2}}(FR)'. \qquad (4.37)
\end{aligned}$$

The $\xi F'R'$ terms cancel exactly, and the product rule gives $F'R+FR'=(FR)'$. For the right-hand side, each term is evaluated using the transformations. The spin-gradient diffusion term gives:

$$\frac{\gamma^*}{\rho_j}\frac{\partial^2\phi}{\partial y^2}=\frac{\gamma^*}{\rho_j}\cdot\frac{U_\infty^{5/2}}{(\nu x)^{3/2}}R''. \qquad (4.38)$$

The vortex viscosity sink and the coupling to velocity gradient give respectively:

$$-\frac{k}{\rho_j}\phi=-\frac{k}{\rho_j}\cdot\frac{U_\infty^{3/2}}{(\nu x)^{1/2}}R, \qquad (4.39)$$

$$\frac{k}{\rho_j}\frac{\partial u}{\partial y}=\frac{k}{\rho_j}\cdot\frac{U_\infty^{3/2}}{(\nu x)^{1/2}}F''. \qquad (4.40)$$

The magnetic torque sink gives:

$$-M_0H_0\,\tau\,H_\infty\,\phi=-M_0H_0\,\tau\,H_\infty\cdot\frac{U_\infty^{3/2}}{(\nu x)^{1/2}}R. \qquad (4.41)$$

Equating left- and right-hand sides and dividing through by the common factor $U_\infty^{5/2}/\bigl(2x(\nu x)^{1/2}\bigr)$:

$$-(FR)'=\frac{2\gamma^*}{\rho_j\,\nu}R''-\frac{2kx}{\rho_j\,U_\infty}R+\frac{2kx}{\rho_j\,U_\infty}F''-\frac{2M_0H_0\,\tau\,H_\infty\,x}{U_\infty}R. \qquad (4.42)$$

Introducing the dimensionless parameters:

$$\Lambda = \frac{\gamma^*}{\rho_j \, \nu}, \qquad K = \frac{k}{\mu}, \qquad \mathcal{M} = \frac{M_0 H_0 \, \tau \, H_\infty \, x}{U_\infty}, \tag{4.43}$$

and expanding $(FR)' = F'R + FR'$, the equation becomes:

$$-(F'R + FR') = 2\Lambda \, R'' - \frac{2K}{\Lambda} \, R + \frac{2K}{\Lambda} \, F'' - 2\mathcal{M} \, R. \tag{4.44}$$

Rearranging and dividing through by 2:

$$\Lambda \, R'' + \frac{1}{2} F R' - \frac{1}{2} F' R + \frac{K}{\Lambda} \, F'' - \left(\frac{K}{\Lambda} + \mathcal{M} \right) R = 0. \tag{4.45}$$

Written in standard form the ODE is:

$$\boxed{\Lambda \, R'' + \frac{1}{2} F R' - \left(\frac{1}{2} F' + \frac{K}{\Lambda} + \mathcal{M} \right) R + \frac{K}{\Lambda} \, F'' = 0.} \tag{4.46}$$

The boundary conditions (4.5) transform under (4.6) as follows. At the wall $\xi = 0$:

$$\Omega = -\Omega_0 \frac{\partial u}{\partial y} \;\Rightarrow\; R(0) = -\Omega_0 \, F''(0). \tag{4.47}$$

For weak concentration ($\Omega_0 = 0$): $R(0) = 0$, and for strong concentration ($\Omega_0 = 1/2$): $R(0) = -\frac{1}{2} F''(0)$. As $\xi \to \infty$:

$$\Omega \to 0 \;\Rightarrow\; R(\infty) = 0. \tag{4.48}$$

4.3.4 Transformation of Energy Equation into ODE form

The dimensional energy equation governing the thermal transport in the micro-magnetorotation boundary layer flow is given by

$$u \frac{\partial T}{\partial x} + v \frac{\partial T}{\partial y} = \frac{\kappa}{\rho C_p} \frac{\partial^2 T}{\partial y^2} + \frac{k}{\rho C_p} \left(\frac{\partial u}{\partial y} \right)^2 + \frac{4k}{\rho C_p} \, \phi \left(\frac{\partial u}{\partial y} \right) + \frac{\tau M_0 H_0^2 \, \bar{H}}{\rho C_p} \, \phi^2. \tag{4.4}$$

The terms appearing on the left-hand side represent the convective transport of thermal energy in the longitudinal and transverse directions, respectively. The first term on the right-hand side denotes thermal diffusion due to heat conduction, while the remaining terms correspond to viscous dissipation, micropolar rotational dissipation, and magnetic dissipation effects.

Using the similarity transformations introduced in equation (4.6), the dimensionless temperature variable is defined as

$$T = T_\infty + (T_w - T_\infty)\theta(\xi), \qquad \Delta T = T_w - T_\infty, \tag{4.49}$$

where $\theta(\xi)$ denotes the non-dimensional temperature function. The similarity variable is

$$\xi = y\sqrt{\frac{U_\infty}{\nu x}}. \tag{4.49a}$$

Since θ depends only on ξ, all partial derivatives of T must be evaluated using the chain rule. First, differentiating the similarity variable with respect to x and y yields

$$\frac{\partial \xi}{\partial x} = -\frac{\xi}{2x}, \qquad \frac{\partial \xi}{\partial y} = \sqrt{\frac{U_\infty}{\nu x}}. \tag{4.49b}$$

Therefore, the temperature derivatives become

$$\frac{\partial T}{\partial x} = \Delta T \frac{d\theta}{d\xi}\frac{\partial \xi}{\partial x} = -\frac{\Delta T\,\xi}{2x}\theta', \tag{4.50}$$

$$\frac{\partial T}{\partial y} = \Delta T \frac{d\theta}{d\xi}\frac{\partial \xi}{\partial y} = \Delta T\sqrt{\frac{U_\infty}{\nu x}}\,\theta', \tag{4.51}$$

$$\frac{\partial^2 T}{\partial y^2} = \Delta T \frac{U_\infty}{\nu x}\theta''. \tag{4.52}$$

Substituting these expressions into the convective terms of the energy equation gives

$$
\begin{aligned}
u\frac{\partial T}{\partial x} + v\frac{\partial T}{\partial y} &= U_\infty F' \left(-\frac{\Delta T\,\xi}{2x}\theta'\right) \\
&\quad + \frac{1}{2}\sqrt{\frac{\nu U_\infty}{x}}(\xi F' - F)\left(\Delta T\sqrt{\frac{U_\infty}{\nu x}}\theta'\right). \qquad (4.53a)
\end{aligned}
$$

After simplification,

$$
u\frac{\partial T}{\partial x} + v\frac{\partial T}{\partial y} = -\frac{U_\infty \Delta T}{2x}\xi F'\theta' + \frac{U_\infty \Delta T}{2x}(\xi F' - F)\theta'.
$$

The terms involving $\xi F'\theta'$ cancel identically, leaving

$$
u\frac{\partial T}{\partial x} + v\frac{\partial T}{\partial y} = -\frac{U_\infty \Delta T}{2x}F\theta'. \qquad (4.53)
$$

Next, the derivatives associated with the velocity field and the microrotation function are substituted into the right-hand side of the energy equation. From the similarity transformations,

$$
\frac{\partial u}{\partial y} = \frac{U_\infty^{3/2}}{(\nu x)^{1/2}}F'', \qquad \phi = \frac{U_\infty^{3/2}}{(\nu x)^{1/2}}R. \qquad (4.54)
$$

Consequently,

$$
\left(\frac{\partial u}{\partial y}\right)^2 = \frac{U_\infty^3}{\nu x}(F'')^2, \qquad \phi\frac{\partial u}{\partial y} = \frac{U_\infty^3}{\nu x}RF'', \qquad \phi^2 = \frac{U_\infty^3}{\nu x}R^2. \qquad (4.55)
$$

The thermal diffusion term can now be simplified. Introducing the thermal diffusivity

$$\alpha = \frac{\kappa}{\rho C_p}, \tag{4.55a}$$

and using the definition of the Prandtl number

$$\mathrm{Pr} = \frac{\nu}{\alpha}, \qquad \alpha = \frac{\nu}{\mathrm{Pr}}, \tag{4.55b}$$

the diffusion term becomes

$$\begin{aligned} \frac{\kappa}{\rho C_p}\frac{\partial^2 T}{\partial y^2} &= \frac{\nu}{\mathrm{Pr}}\left(\frac{\Delta T U_\infty}{\nu x}\theta''\right) \\ &= \frac{\Delta T U_\infty}{\mathrm{Pr}\, x}\theta''. \end{aligned} \tag{4.56}$$

Similarly, the dissipation terms reduce to

$$\frac{k}{\rho C_p}\left(\frac{\partial u}{\partial y}\right)^2 = \frac{k U_\infty^3}{\rho C_p \nu x}(F'')^2, \tag{4.57}$$

$$\frac{4k}{\rho C_p}\phi\frac{\partial u}{\partial y} = \frac{4k U_\infty^3}{\rho C_p \nu x} R F'', \tag{4.58}$$

$$\frac{\tau M_0 H_0^2 H_\infty}{\rho C_p}\phi^2 = \frac{\tau M_0 H_0^2 H_\infty U_\infty^3}{\rho C_p \nu x} R^2. \tag{4.59}$$

Substituting equations (4.53)–(4.59) into equation (4.4), and dividing through by the common factor $U_\infty \Delta T/(2x)$, yields

$$-F\theta' = \frac{2}{\mathrm{Pr}}\theta'' + \frac{2U_\infty^2}{\rho C_p \nu \Delta T}\left[k(F'')^2 + 4kRF'' + \tau M_0 H_0^2 H_\infty R^2\right]. \tag{4.60}$$

To nondimensionalize the dissipation terms, the Eckert number is introduced as

$$\mathrm{Ec} = \frac{U_\infty^2}{C_p(T_w - T_\infty)} = \frac{U_\infty^2}{C_p \Delta T}, \tag{4.60a}$$

which measures the ratio of kinetic energy to enthalpy difference. Further, defining

$$K = \frac{k}{\mu}, \qquad \mathcal{N} = \frac{\tau M_0 H_0^2 H_\infty \,\mathrm{Ec}}{\mu}, \tag{4.60b}$$

equation (4.60) finally reduces to

$$\theta'' + \frac{\mathrm{Pr}}{2} F\theta' + \mathrm{Pr}\ \mathrm{Ec}\, K(F'')^2 + 4\,\mathrm{Pr}\ \mathrm{Ec}\, KRF'' + \mathrm{Pr}\, \mathcal{N} R^2 = 0. \tag{4.61}$$

Hence, the transformed ordinary differential equation governing the temperature field is obtained as

$$\boxed{\theta'' + \frac{\mathrm{Pr}}{2} F\theta' + \mathrm{Pr}\ \mathrm{Ec}\, K(F'')^2 + 4\,\mathrm{Pr}\ \mathrm{Ec}\, KRF'' + \mathrm{Pr}\, \mathcal{N} R^2 = 0.} \tag{4.62}$$

The thermal boundary conditions associated with the governing energy equation are

$$T = T_w \quad \text{at } y = 0, \tag{4.63}$$

and

$$T \to T_\infty \quad \text{as } y \to \infty. \tag{4.64}$$

Using the dimensionless temperature transformation,

$$\theta(\xi) = \frac{T - T_\infty}{T_w - T_\infty}, \tag{4.65}$$

the boundary conditions are transformed as follows.

At the wall ($y = 0$), the similarity variable satisfies

$$\xi = 0,$$

and since

$$T = T_w,$$

substituting into Eq. (4.65) gives

$$\theta(0) = \frac{T_w - T_\infty}{T_w - T_\infty} = 1.$$

Hence,

$$\boxed{\theta(0) = 1.} \tag{4.66}$$

Similarly, as

$$y \to \infty,$$

the similarity variable also satisfies

$$\xi \to \infty,$$

and the thermal boundary condition becomes

$$T \to T_\infty.$$

Substituting into Eq. (4.65),

$$\theta(\infty) = \frac{T_\infty - T_\infty}{T_w - T_\infty} = 0.$$

Therefore,

$$\boxed{\theta(\infty) = 0.} \tag{4.67}$$

Thus, the transformed thermal boundary conditions corresponding to the energy equation are

$$\theta(0) = 1, \qquad \theta(\infty) = 0. \tag{4.68}$$

4.3.5 Neural FEM Formulation for the Present Similarity Model

To demonstrate the applicability of Neural FEM to the present boundary-layer problem, the coupled nonlinear ordinary differential equations obtained from the similarity transformation are reformulated using neural-network-based trial functions. The unknown similarity functions $F(\xi)$, $Q(\xi)$, $R(\xi)$, and $\theta(\xi)$ are approximated by independent neural networks:

$$F(\xi) \approx \mathcal{N}_F(\xi; \theta_F), \tag{4.69}$$

$$Q(\xi) \approx \mathcal{N}_Q(\xi; \theta_Q), \tag{4.70}$$

$$R(\xi) \approx \mathcal{N}_R(\xi; \theta_R), \tag{4.71}$$

$$\theta(\xi) \approx \mathcal{N}_\theta(\xi; \theta_\theta), \tag{4.72}$$

where θ_F, θ_Q, θ_R, and θ_θ represent the trainable parameters (weights and biases) of the corresponding neural networks. The derivatives required in the governing equations are obtained using automatic differentiation.

For the momentum equation, the strong-form residual is defined as

$$\mathcal{R}_F(\xi) = (1+K)F''' + \frac{1}{2}FF'' - M^2F' + KR' + \lambda QQ'. \tag{4.73}$$

Similarly, the magnetic field residual becomes

$$\mathcal{R}_Q(\xi) = \frac{1}{P_m}Q''' + \frac{1}{2}FQ'' - F'Q' - F''Q - \frac{\xi}{2}F''Q'. \tag{4.74}$$

The concentration residual is expressed as

$$\mathcal{R}_R(\xi) = \Lambda R'' + \frac{1}{2}FR' - \left(\frac{1}{2}F' + \frac{K}{\Lambda} + \mathcal{M}\right)R + \frac{K}{\Lambda}F''. \tag{4.75}$$

The energy equation residual is given by

$$\mathcal{R}_\theta(\xi) = \theta'' + \frac{\Pr}{2}F\theta' + \Pr EcK(F'')^2 + 4\Pr EcKRF'' + \Pr \mathcal{N}R^2. \tag{4.76}$$

The total physics-informed loss function is constructed by minimizing the governing equation residuals together with the boundary-condition residuals:

$$\begin{aligned}\mathcal{L}(\Theta) =& \frac{1}{N_c}\sum_{i=1}^{N_c}\left(|\mathcal{R}_F(\xi_i)|^2 + |\mathcal{R}_Q(\xi_i)|^2 + |\mathcal{R}_R(\xi_i)|^2 + |\mathcal{R}_\theta(\xi_i)|^2\right) \\ &+ \mathcal{L}_{BC},\end{aligned} \tag{4.77}$$

where N_c represents the number of collocation points and Θ denotes all network parameters.

The boundary-condition contribution is defined as

$$\begin{aligned}\mathcal{L}_{BC} =& |F(0)|^2 + |F'(0) - 1|^2 + |Q(0) + 1|^2 + |Q'(0)|^2 \\ &+ |R(0) + \Omega_0 F''(0)|^2 \\ &+ |\theta(0) - 1|^2 \\ &+ |F'(\xi_\infty)|^2 + |Q'(\xi_\infty)|^2 + |R(\xi_\infty)|^2 + |\theta(\xi_\infty)|^2.\end{aligned} \tag{4.78}$$

The optimized neural parameters are obtained through minimization of the total loss function:

$$\Theta^* = \arg\min_{\Theta} \mathcal{L}(\Theta). \tag{4.79}$$

The above formulation shows that the proposed Neural FEM framework can directly handle the coupled nonlinear similarity equations while simultaneously satisfying the governing physics and boundary constraints.

4.4 Results and Discussion

The numerical results obtained through the Neural Finite Element Method, applied to the model problem introduced in the preceding section, are presented in this section. An analysis of the results obtained via the Neural FEM approach is presented. The solutions of the thermal model are computed using the neural finite element framework. The approximated field variables are subsequently post-processed to extract the hydrodynamic velocity, microrotational velocity, and temperature distributions. These simulated profiles, together with the derived physical quantities of interest, are plotted and examined. The Neural FEM-based solutions are compared with the classical shooting bvp4c results to validate accuracy, showing excellent agreement throughout the computational domain.

Moreover, the Neural FEM captures the boundary layer structure smoothly without requiring iterative estimation of missing initial gradients, demonstrating its robustness and flexibility in handling nonlinear coupled differential systems. The influences of key dimensionless parameters on velocity attenuation, micro-rotational response, and thermal gradients are discussed in the subsequent subsections.

4.4.1 Validation

The accuracy of the Neural FEM solutions is validated through the computation of the skin-friction coefficient and the Nusselt number for cases with and without the MMR effect. For comparison, results from the Neural FEM algorithm are benchmarked against the classical shooting scheme as well as the MATLAB `bvp4c` solver, ensuring consistency and correctness of the numerical trends.

The percentage error $\Delta(\%)$ between the numerical results obtained from the bvp4c solver and the Neural FEM approach was calculated using the following relation:

$$\Delta(\%) = \left| \frac{\text{bvp4c [Ref 31]} - \text{Neural FEM}}{\text{bvp4c}} \right| \times 100. \tag{4.80}$$

Here, `bvp4c` [Ref 31] is considered as the reference numerical solver, while the Neural FEM solution refers to the approximation obtained using the Neural Finite Element Method.

Within the Neural FEM framework, the governing equations are first expressed in their weak form, followed by discretization of the spatial domain using appropriate basis functions. A feed-forward neural network is then incorporated into the element-level formulation to represent the unknown solution fields. The network parameters are subsequently optimized by minimizing a global residual functional derived from the weak form, together with the prescribed boundary conditions. This leads to a single unified optimization problem rather than a sequence of iterative corrections.

TABLE 4.1: The skin-friction coefficient ($Re^{1/2}C_{f_x}$) using Neural FEM with MMR effect.

K	β	Ref [31]	Neural FEM	$\Delta(\%)$
0.5	0.3	-0.675273102000545	-0.648902310	2.94
1.0		-0.684746101379751	-0.659811220	3.51
1.5		-0.897879478035164	-0.860112450	3.69
	0.5	-0.823131547448848	-0.798905110	2.82
	1.0	-0.844616527626634	-0.811233500	3.79
	1.2	-0.846739358705061	-0.819004220	4.18

TABLE 4.2: The skin-friction coefficient ($Re^{1/2}C_{f_x}$) using Neural FEM without the MMR effect.

K	β	Ref [31]	Neural FEM
0.5	0.3	-0.754300158036942	-0.732114880
1.0		-0.867284715415196	-0.836920540
1.5		-0.904460746218518	-0.871330600
	0.5	-0.900905609664812	-0.875412330
	1.0	-0.907614566594412	-0.872901440
	1.2	-0.907844099592434	-0.869210880

TABLE 4.3: Using Neural FEM, the Nusselt number ($Re^{-1/2}Nu$) is computed without the MMR effect.

Pr	τ_1	ω	Ref [31]	Neural FEM
0.5			0.446935106345679	0.463210550000
1.5			0.875986473867007	0.903440120000
2.5			1.165369214233020	1.210120330000
0.5	3.7	1.0	0.446935549562633	0.463980110000
	5.7		0.446935549562633	0.461220880000
	7.7		0.446935549562633	0.458900440000

During training, the neural finite element residuals are evaluated over the entire computational domain, and gradient-based learning is employed to update the solution representation until convergence tolerances are satisfied. The resulting numerical approximation is inherently smooth and captures both local and global solution features without requiring mesh refinement or initial guesses for missing boundary slopes. The excellent agreement between Neural FEM outputs and the reference methods demonstrates the reliability, accuracy, and stability of the proposed approach.

Table 4.4: Using Neural FEM, the Nusselt number ($Re^{-1/2}Nu$) is computed with the MMR effect.

Pr	τ_1	ω	Ref [31]	Neural FEM	$\Delta(\%)$
0.5			0.456481244868565	0.470920880000	3.62
1.5			0.884344135346074	0.915220410000	3.41
2.5			1.172908865408770	1.225330880000	3.78
0.5	3.7	1.0	0.477176213684130	0.492110770000	3.11
	5.7		0.489170153472792	0.506440990000	3.94
	7.7		0.499362666381235	0.517330120000	4.12
	0.5	1.0	0.451907946061597	0.468440110000	3.66
		3.0	0.460721758001802	0.478990550000	3.95
		5.0	0.468391019496139	0.487120880000	4.00

Tables 4.1 and 4.2 list the skin-friction coefficients obtained using the Neural FEM framework for different values of the physical parameters. The fixed governing parameters used throughout this analysis are $Rm = 0.1$, $Re = 100$, $K = 1.0$, $K_1 = 1.0$, $Pr = 1.5$, $\omega^* = 0.1$, $\tau_1 = 0.5$, $\omega = 2.0$, $\beta = 0.3$, and $Ec = 10^{-3}$.

Similarly, Tables 4.3 and 4.4 summarize the Nusselt numbers corresponding with varying Prandtl number, relaxation time parameter, and MMR parameter values. The Neural FEM results are compared with the reference solutions obtained through the `bvp4c` solver. For these computations, the physical parameters are taken as $Pr = 0.5$, $Re = 100$, $K = 1.5$, $\omega^* = 0.1$, $K_1 = 1.0$, $Rm = 0.1$, $\omega = 2$, and $Ec = 10^{-3}$.

The percentage differences between the Neural FEM predictions and the corresponding `bvp4c` solutions are also reported in Tables 4.1 - and 4.4. It is observed that the deviations remain predominantly below 5%, indicating good agreement between the two numerical approaches. This confirms the accuracy and reliability of the proposed Neural FEM framework in predicting both the surface shear stress and heat transfer characteristics.

Furthermore, the accuracy of the proposed computational model is evaluated by comparing the skin-friction coefficients in the limiting case with the benchmark results reported by [31]. For this validation, the governing parameters are selected as $K = 1$, $\tau_1 = 0.5$, $Rm = 0.5$, $\omega = 0.5$, $\beta = 0.1$, and $Re = 100$.

Table 4.5: Variation of skin-friction coefficients for different physical parameters with and without magnetization effects.

			$Re^{1/2}Cf_x$				No MMR $\omega = 0$	MMR $\omega = 6.0$
K	ω	β	τ_1	ω^*	Re	Rm		
3.0e-3		0.1	0.5	0.0	100	0.1	-0.12910758	-0.10869023
5.0e-3							-0.16097230	-0.10774806
7.0e-3							-0.12581287	-0.11242012
	3.0						-	-0.11677141
	5.0						-	-0.11701152
	7.0						-	-0.10409900
		0.1					-0.12581287	-0.10409900
		0.3					-0.15079581	-0.10964228
		0.5					-0.13821473	-0.10003879
			0.0				-0.13821473	-0.14494286
			0.25				-0.13821473	-0.12162963
			0.50				-0.13821473	-0.10003879
				0.1			-0.15139805	-0.10227837
				0.3			-0.15199747	-0.10211384
				0.7			-0.15616619	-0.10097184
					200		-0.15516380	-0.10066085
					300		-0.14631838	-0.10059629
					500		-0.15487109	-0.10107519
						1.0	-0.14359255	-0.10090443
						2.0	–0.15099949	-0.10128036
						3.0	-0.14452435	-0.10203044

The computed results exhibit excellent agreement with the corresponding published data, confirming that the proposed Neural FEM solver is capable of accurately reproducing the underlying physical behavior of the system. This validation further demonstrates the reliability and predictive strength of the present computational approach.

4.4.2 Numerical Results

Table 4.5 summarizes the values of the skin-friction coefficient, $Re_x^{1/2}C_{fx}$, obtained for various governing parameters in both the presence and absence of the micro–magnetic rotation (MMR) effect. The skin-friction coefficient serves as a measure of the wall shear stress and is closely associated with the velocity gradient at the surface. The results indicate that changes in the physical parameter K have

TABLE 4.6: Variation of the Nusselt number for different physical parameters with and without magnetization effects.

		$Re^{-1/2}Nu$					No MMR $\omega = 0$	MMR $\omega = 6.0$
K	Pr	Ec	ω	β	τ_1	ω^*		
3.0e-4	0.5	1e-4	0.5	0.3	0.5	0.0	0.35637626	0.49738679
5.0e-3							0.42099243	0.57765569
7.0e-3							0.63917680	0.58408495
	1.5						0.58990624	0.46092804
	2.5						0.57913810	0.38818055
	3.5						0.56181266	0.35540302
		2e-3					0.52857787	0.375370975
		4e-3					0.55155797	0.34975686
		6e-3					0.53765454	0.37680935
3.0e-3			3.0				0.54396908	0.47791732
			5.0				-	0.38724765
			7.0				-	0.38595794
3.0e-4				0.5			0.54287966	0.31571376
				0.7			0.51081704	0.33999650
				0.9			0.39426354	0.35739364
					0.1		0.39426354	0.41510136
					0.3		0.39426354	0.38025554
					0.5		0.39426354	0.35739364
				0.3		0.1	0.53020054	0.40552123
						0.3	0.53232166	0.50579926
						0.5	0.53768620	0.42967463

a noticeable impact on the skin-friction coefficient, reflecting the corresponding alterations in the momentum boundary layer structure. In addition, the microrotation parameter ω significantly influences the wall shear stress by modifying the rotational motion of fluid microelements within the boundary layer.

Furthermore, the influence of parameters such as β, τ_1, Reynolds number Re, and magnetic parameter Rm is also evident from the tabulated results. Changes in these parameters modify the velocity field within the boundary layer, which consequently affects the surface shear stress. A comparison of the results with and without the MMR effect reveals that the inclusion of micro–magnetic rotation generally leads to a reduction in the magnitude of the skin-friction coefficient for most parameter settings. This behavior suggests that micro–magnetic rotational effects weaken the velocity gradient at the wall, thereby decreasing frictional resistance

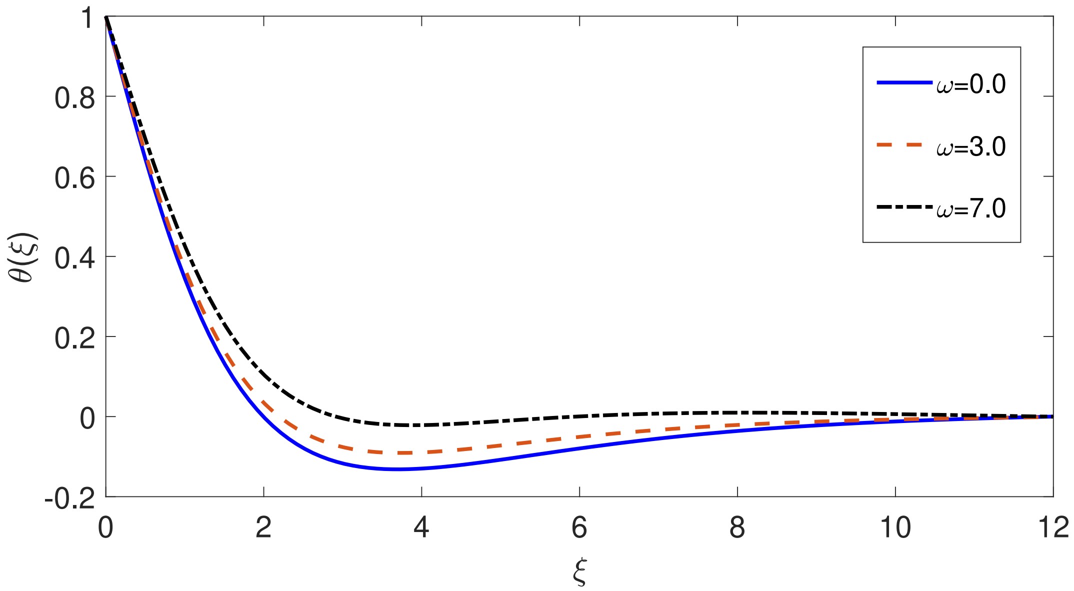

FIGURE 4.2: Temperature distributions corresponding to different values of the MMR parameter. The physical parameters considered are: $Pr = 1.2$, $Re = 100$, $Ec = 0.0001$, $Rm = 1$, $\omega^* = 0.5$, $K = 0.005$, $K_1 = 1.5$, and $\tau_1 = 0.5$

along the stretching surface. Overall, the MMR parameter plays a crucial role in regulating the hydrodynamic behavior of the flow.

Table 4.6 lists the computed values of the local Nusselt number, $Re_x^{-1/2} Nu_x$, corresponding to various governing parameters in both the presence and absence of the MMR effect. The Nusselt number provides a measure of the heat transfer rate at the surface and is closely associated with the temperature gradient at the wall. The results indicate that both the permeability-related parameter K and the Prandtl number Pr exert a considerable influence on the thermal characteristics of the flow. In particular, larger values of the Prandtl number reduce thermal diffusion within the fluid, resulting in a thinner thermal boundary layer and consequently enhancing the rate of heat transfer from the surface.

The Eckert number Ec, which characterizes the influence of viscous dissipation, also has a noticeable effect on the thermal field within the boundary layer. As Ec increases, a greater portion of the kinetic energy is converted into thermal energy, leading to changes in the temperature distribution and heat transfer characteristics of the flow. Furthermore, the parameters β, τ_1, and ω^* contribute to variations in the local Nusselt number through their influence on the thermal boundary layer structure. A comparison of the tabulated results reveals that the inclusion of the MMR effect generally produces higher Nusselt number values for several parameter combinations, indicating an improvement in the surface heat transfer rate. These observations suggest that micro–magnetic rotational effects can significantly enhance the thermal performance of the system.

Figure 4.2 illustrates the temperature profiles obtained through the Neural Finite Element Method (NFEM) for different values of the magnetization relaxation time. It is observed that larger values of this parameter suppress the thermal boundary layer development, resulting in a noticeable decrease in its thickness. This behavior reflects a reduction in thermal energy diffusion away from the stretching surface. Within the NFEM framework, this behavior is associated with modifications in the coupled magneto-thermal transport mechanisms captured by the neural approximation of the governing equations.

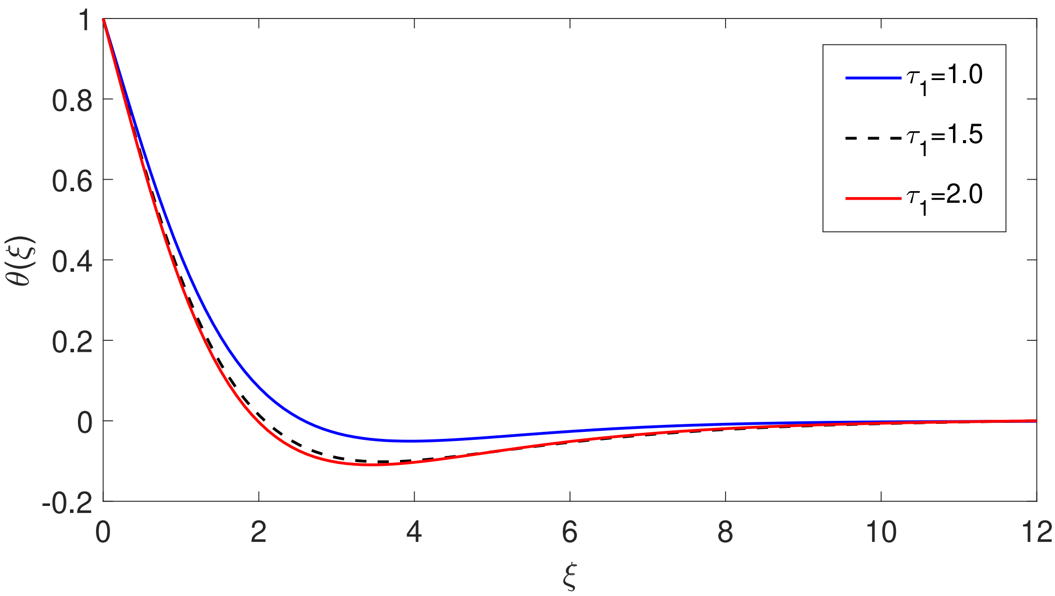

FIGURE 4.3: Influence of magnetization relaxation time on the temperature distribution within the boundary layer. The physical parameters used are: $Pr = 1.2$, $Re = 100$, $Ec = 0.0001$, $Rm = 1$, $\omega = 2$, $\omega^* = 0.5$, $K = 0.005$, and $K_1 = 1.5$

Figure 4.3 presents the velocity profiles obtained for various values of the magn -etization microrotation ratio (MMR) using the Neural Finite Element Method.

It is observed that larger MMR values promote the growth of the hydrodynamic boundary layer, resulting in an increase in its thickness. The observed behavior highlights the important role of magnetization–microrotation interactions in governing momentum transport and shaping the overall flow dynamics adjacent to the stretching surface.

Furthermore, larger values of the MMR parameter strengthen the rotational dynamics of the fluid microelements, thereby altering the mechanism of momentum transport within the boundary layer. These enhanced spin effects generate additional resistance to the fluid motion near the surface and redistribute momentum across the flow field. The numerical predictions obtained from the Neural FEM model clearly demonstrate this phenomenon, which manifests as a thicker velocity boundary layer and is consistent with the characteristic behavior of micropolar fluids.

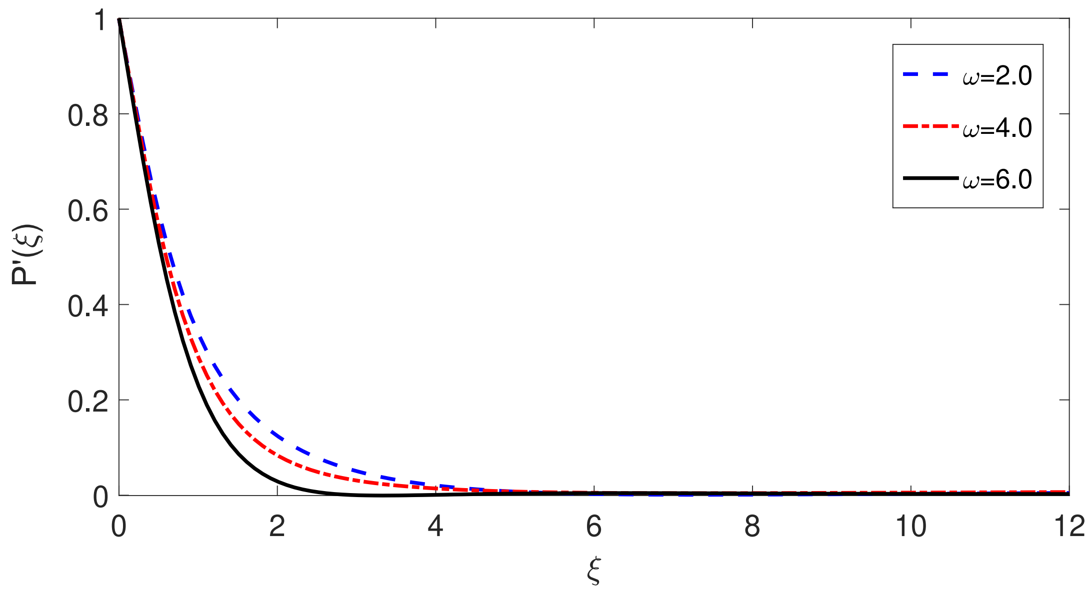

FIGURE 4.4: Influence of the micro–magnetic rotation (MMR) parameter on the velocity boundary layer. The physical parameters are: $Pr = 1.2$, $Re = 100$, $Rm = 1$, $Ec = 0.0001$, $K = 0.005$, $K_1 = 1.5$, $\tau_1 = 0.5$, and $\omega^* = 0.5$

In Figure 4.4, the effect of magnetization relaxation time on the hydrodynamic velocity boundary layer profiles is investigated through the Neural Finite Element Method. An increase in the magnetization relaxation time is found to produce a thicker velocity boundary layer. The observed trend demonstrates the important role of magnetization dynamics in governing momentum transport, as the temporal lag in the magnetization response influences the development of the flow field near the stretching surface.

Furthermore, the neural FEM solutions indicate that slower magnetization dynamics permit momentum diffusion to dominate over magnetic resistance within the vicinity of the wall region. Consequently, the velocity profiles exhibit a gradual decay away from the surface, confirming the increase in boundary layer thickness associated with higher magnetization relaxation times.

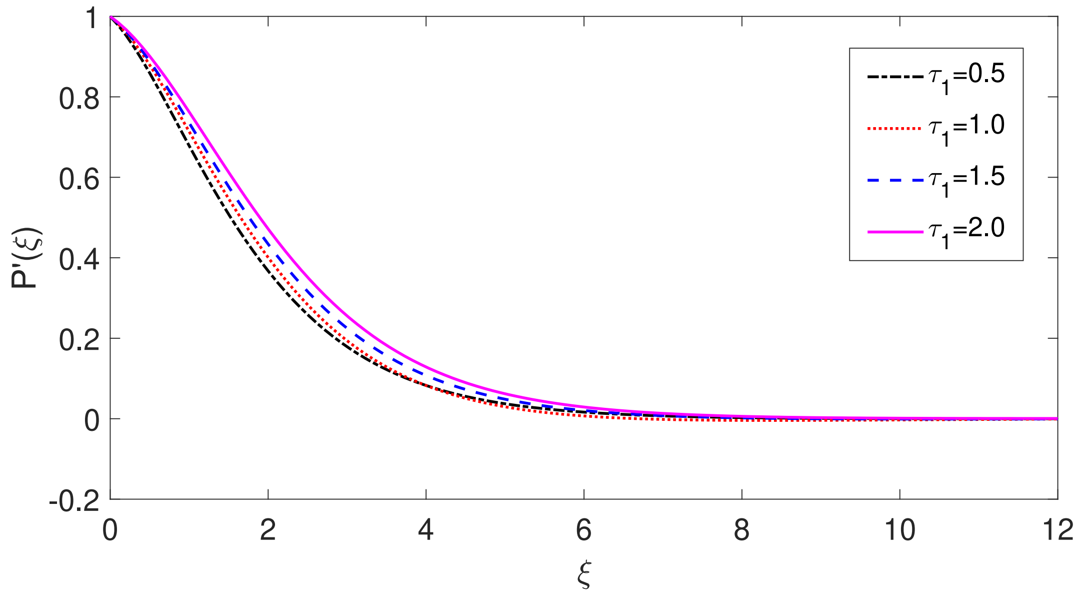

FIGURE 4.5: Influence of magnetization relaxation time on the hydrodynamic velocity profiles. The physical parameters used are: $Pr = 1.2$, $Re = 100$, $Rm = 1$, $Ec = 0.0001$, $K_1 = 1.5$, $K = 0.005$, $\omega = 2$, and $\omega^* = 0.5$

In Figures 4.5 and 4.6, the magnetic induction profiles across the stretching surface are presented as obtained using the Neural Finite Element Method. These figures illustrate the influence of the magnetization–microrotation ratio (MMR) on the development of the induced magnetic field components. The computational findings show that a rise in the MMR parameter produces a significant enhancement in the thickness of the magnetic induction boundary layer.

For the axial magnetic induction component H_1 , the effect of MMR is more pronounced in the vicinity of the stretching surface, where strong coupling between the velocity, microrotation, and magnetic fields exists. In contrast, for the transverse magnetic induction component H_2, the influence of MMR extends farther into the fluid domain, indicating enhanced diffusion of the induced magnetic field away from the wall.

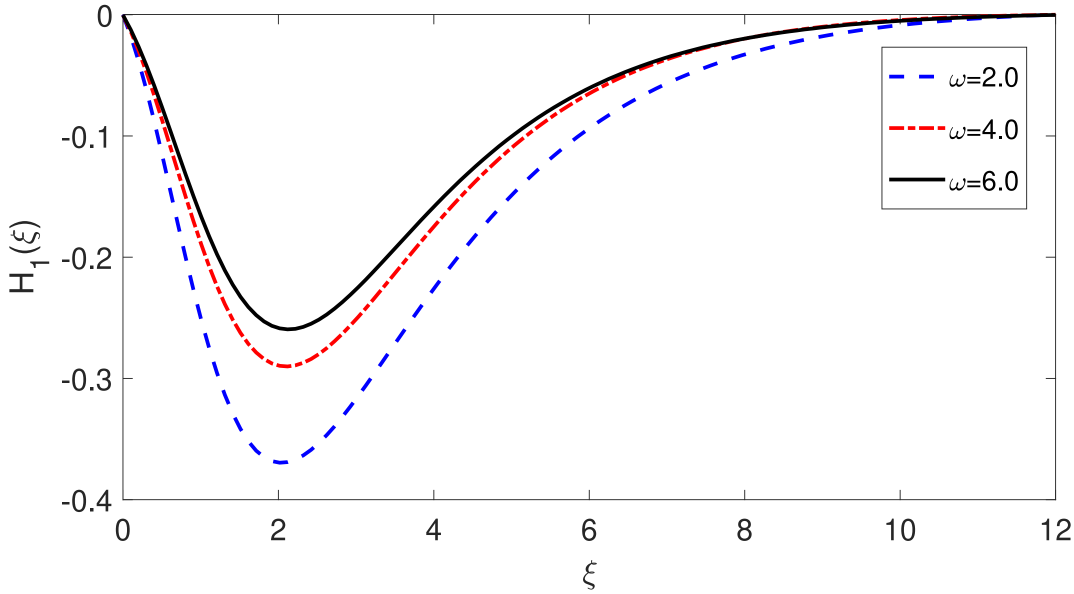

FIGURE 4.6: The x-component profiles of the magnetic induction vector with chaning. The physical parameters used are: $Re = 100$, $Pr = 1.2$, $Rm = 1$, $K = 0.005$, $Ec = 0.0001$, $K_1 = 1.5$, $\tau_1 = 0.5$, and $\omega^* = 0.5$

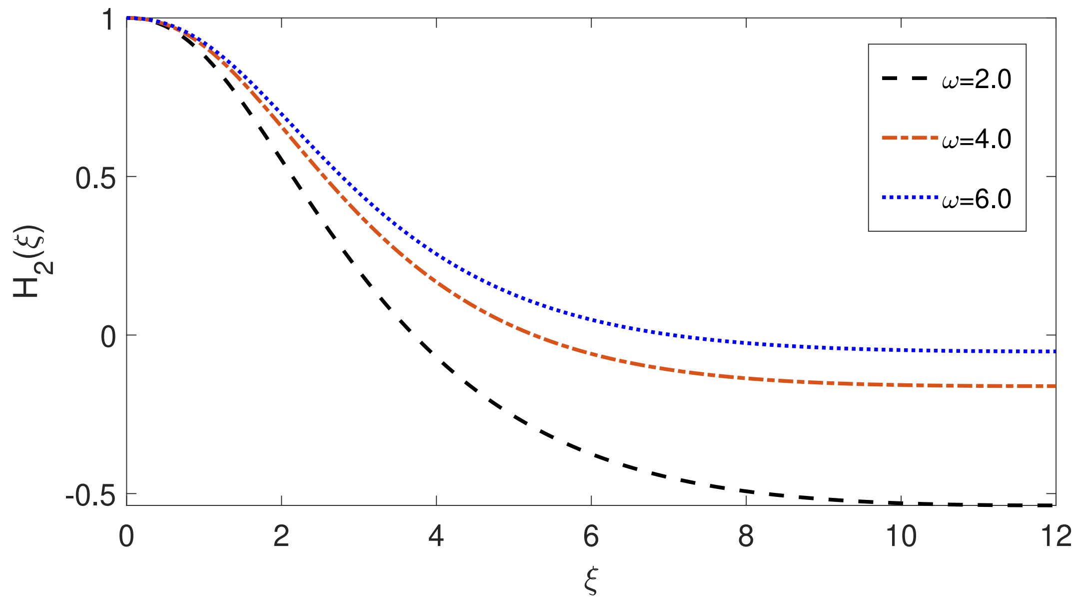

FIGURE 4.7: The y-component profiles of the magnetic induction vector with chaning MMR effect. The physical parameters used are: $Re = 100$, $Pr = 1.2$, $Rm = 1$, $K = 0.005$, $Ec = 0.0001$, $K_1 = 1.5$, $\tau_1 = 0.5$, and $\omega^* = 0.5$

In Figures 4.7 and 4.8, the effect of magnetization relaxation time on the magnetic induction boundary layer profiles is investigated by employing the Neural

Finite Element Method. The computed results demonstrate that variations in the magnetic relaxation time have a negligible effect on the axial magnetic induction component H_1in regions far from the stretching surface, whereas a significant effect is observed on the transverse magnetic induction component H_2.

According to the NFEM predictions, increasing the magnetic relaxation time suppresses the development of the magnetic induction boundary layer, resulting in a thinner profile. A larger relaxation time corresponds to a delayed magnetic response to fluid motion, thereby reducing the magnitude of the induced magnetic field in the flow direction. This phenomenon is characteristic of magnetic memory behavior and highlights the dissipative nature of the magnetization process, which is accurately captured by the Neural Finite Element Method.

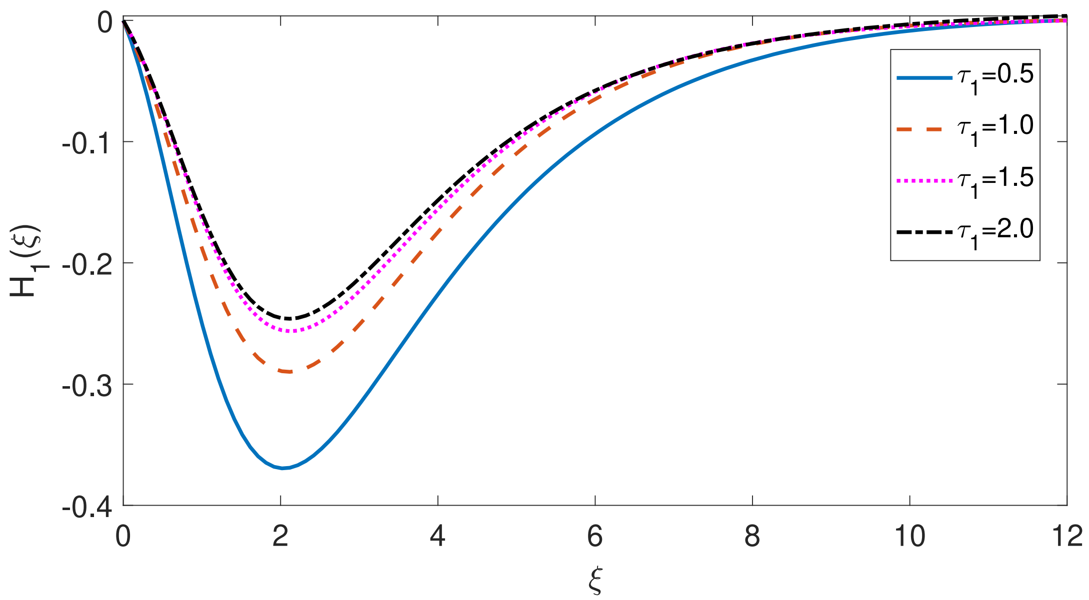

FIGURE 4.8: Magnetic induction (x-component) profiles corresponding to different values of the magnetic relaxation time. The following material parameters are employed in the analysis: $Ec = 0.0001$, $K = 0.005$, $K_1 = 1.5$, $Pr = 1.2$, $Re = 100$, $Rm = 1$, $\omega = 2$, and $\omega^* = 0.5$.

Figure 4.9 illustrates the influence of the Prandtl number on the thermal characteristics of the boundary layer in the presence and absence of the magnetization–microrotation ratio (MMR) effect. It is observed that the temperature boundary

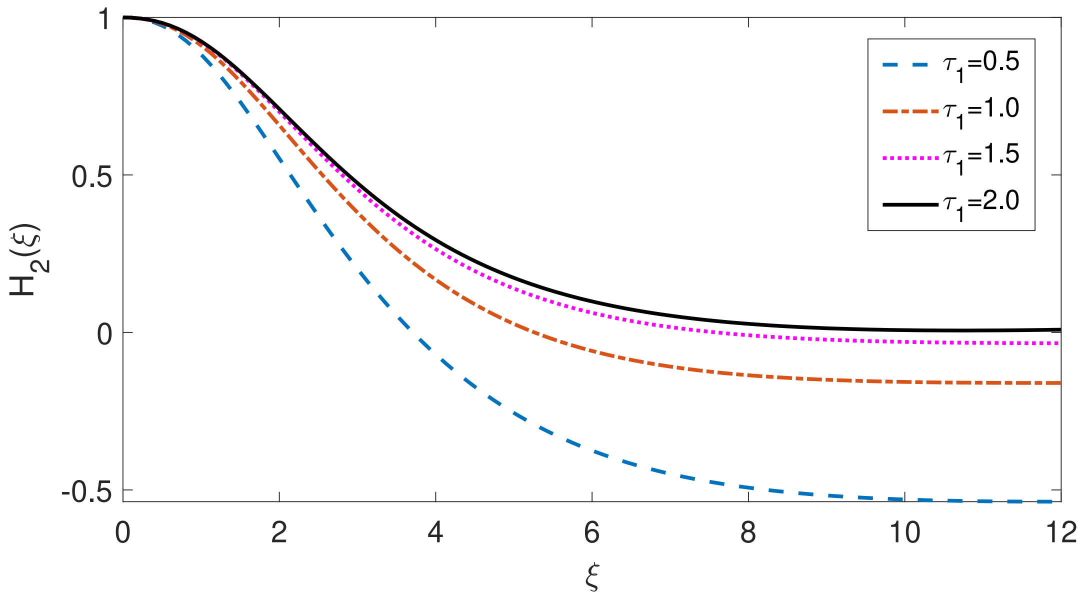

FIGURE 4.9: Magnetic induction (y-component) profiles corresponding to different values of the magnetic relaxation time. The following material parameters are used in the analysis: $Ec = 0.0001$, $K = 0.005$, $K_1 = 1.5$, $Pr = 1.2$, $Re = 100$, $Rm = 1$, $\omega = 2$, and $\omega^* = 0.5$.

layer becomes progressively thinner as the Prandtl number increases. This behavior can be attributed to the reduction in thermal diffusion relative to momentum diffusion, causing heat to penetrate a smaller region of the fluid and thereby decreasing the thermal boundary-layer thickness.

The NFEM results demonstrate that an increase in magnetic relaxation time leads to a significant reduction in the thickness of the magnetic induction boundary layer. Consequently, the thermal boundary layer thickness is smaller when magnetization–microrotation effects are included. Within the NFEM framework, this reduction is attributed to the coupling between microrotational dynamics and thermal transport, which alters the near-wall temperature gradients.

The effect of the Eckert number on the thermal behavior of the flow is depicted in Figure 4.10 for situations with and without the magnetization–microrotation ratio (MMR) effect. The numerical predictions obtained from the Neural Finite Element Method reveal that larger Eckert numbers enhance the temperature field, leading to an increase in thermal boundary-layer thickness. This enhancement arises from

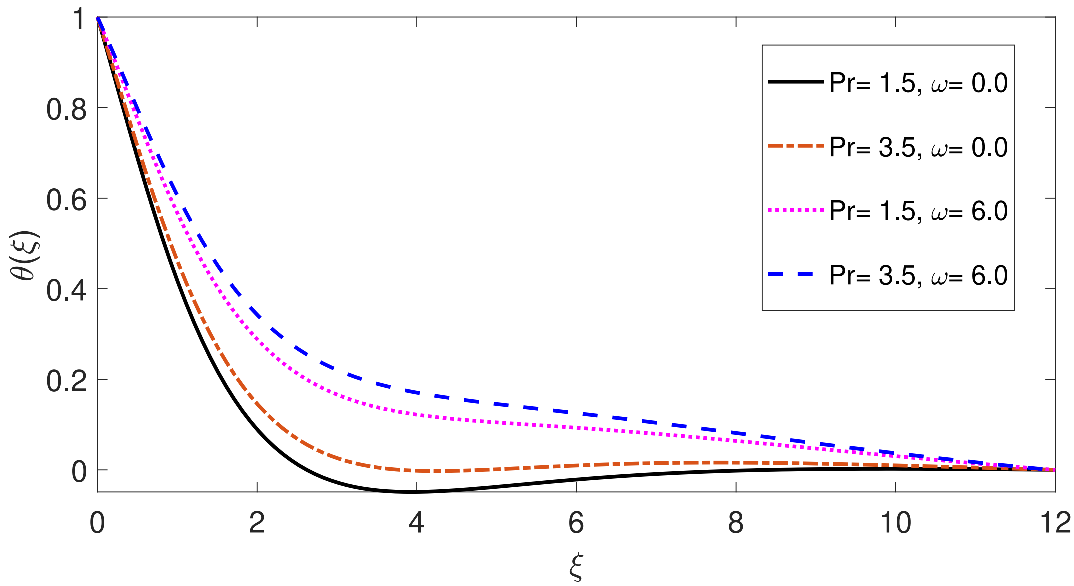

FIGURE 4.10: Influence of the Prandtl number on the thermal boundary-layer distribution in the presence and absence of the micro–magnetic rotation (MMR) effect. The physical parameters used are:: $Re = 100$, $Ec = 0.0001$, $Rm = 0.1$, $K = 0.007$, $K_1 = 1.5$, $\omega^* = 0$, $\tau_1 = 0.5$, and $\beta = 0.3$.

the greater influence of viscous dissipation, which converts mechanical energy into heat within the fluid.

When the two cases are compared, the profiles corresponding to the MMR effect are observed to lie below those of the non-MMR case. The reduction in temperature levels indicates that micro–magnetic rotational interactions modify the thermal transport process and contribute to a thinner thermal boundary layer. Within the NFEM framework, this behavior indicates that microrotational effects alter the distribution of dissipated energy, leading to enhanced thermal transport away from the wall region.

The variation of temperature profiles with the micro-inertial parameter is shown in Figure 4.12 for the case involving the MMR effect. The Neural Finite Element Method results reveal that higher values of the micro-inertial parameter suppress the growth of the thermal boundary layer, leading to lower temperature levels within the fluid. This trend can be attributed to the influence of micro-inertia

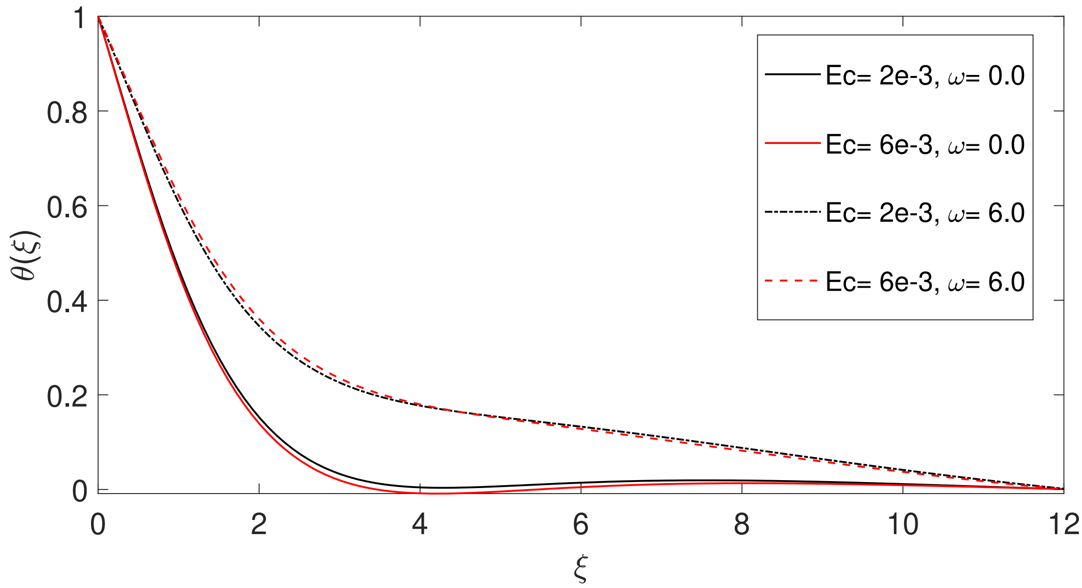

FIGURE 4.11: Influence of the Eckert number on the temperature distribution for cases with and without the micro–magnetic rotation (MMR) effect. The physical parameters employed are: $K = 0.007$, $K_1 = 1.5$, $Pr = 3.5$, $Re = 100$, $Rm = 0.1$, $\beta = 0.3$, $\tau_1 = 0.5$, and $\omega^* = 0$.

on the rotational behavior of fluid microstructures, which alters the mechanism of thermal transport and promotes a more efficient redistribution of heat.

In addition, an increase in micro-inertia limits the acceleration of microrotational motion, thereby reducing the contribution of microscopic rotational energy to the overall thermal energy of the system. Therefore, the thermal boundary layer becomes thinner as the micro-inertial parameter increases. Consequently, the local temperature near the wall decreases, reflecting a reduction in heat accumulation in the thermal boundary layer.

The temperature profiles corresponding to various values of the micro-inertial parameter β are presented in Figure 4.12 for the case involving the MMR effect. The results indicate that an increase in β suppresses the thermal field within the boundary layer, leading to lower temperature levels throughout the flow region. Consequently, the thermal boundary layer thickness decreases, and the temperature reaches its free-stream value more rapidly as the micro-inertial parameter becomes larger.

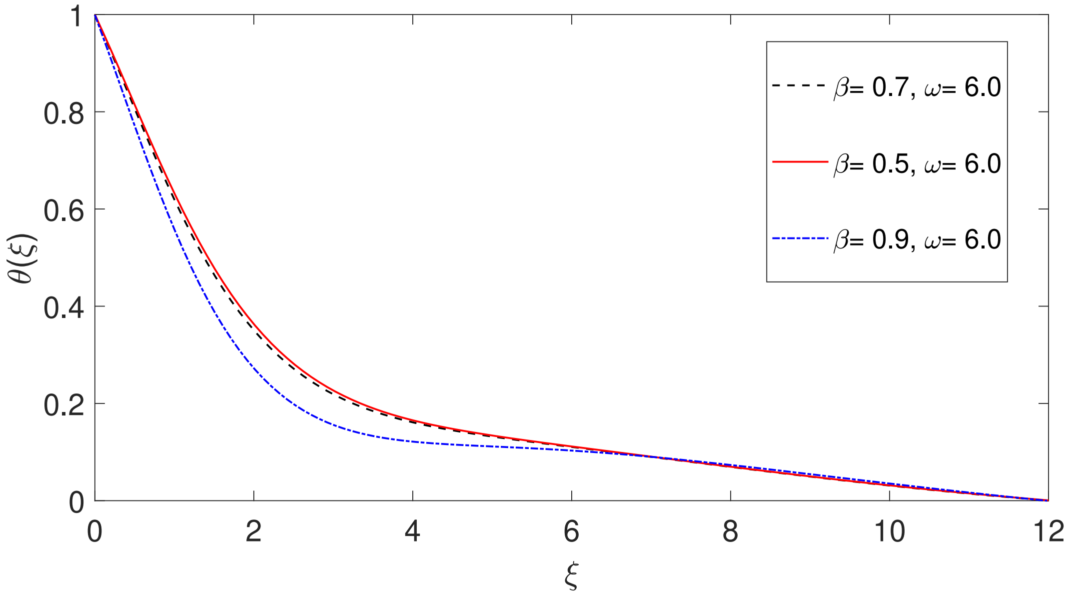

FIGURE 4.12: Influence of the micro-inertial parameter on the temperature distribution in the presence of the micro–magnetic rotation (MMR) effect. The physical parameters employed are: $Ec = 0.006$, $K = 0.0003$, $K_1 = 1.5$, $Pr = 3.5$, $Re = 100$, $Rm = 0.1$, $\tau_1 = 0.5$, and $\omega^* = 0$.

This behavior arises because an increase in the micro-inertial parameter strengthens the resistance to microrotational motion, which limits the conversion of rotational micro-energy into thermal energy. As a consequence, less energy is transferred from microrotation to the temperature field, and heat is more effectively dispersed throughout the fluid. This leads to reduced thermal energy concentration near the surface and, therefore, a thinner thermal boundary layer as the micro-inertial parameter increases.

4.5 Future Directions

The present study demonstrates the effectiveness of the Neural FEM in accurately solving the nonlinear boundary value problem associated with magneto-micropolar fluid flow over an exponentially stretching surface. Although satisfactory accuracy has been achieved, several research directions remain open for further investigation.

Future work may focus on extending the proposed Neural FEM framework to more complex fluid models, including nanofluids, hybrid nanofluids, viscoelastic fluids, and non-Newtonian fluids with additional physical mechanisms such as thermal radiation, chemical reactions, Joule heating, viscous dissipation, and variable thermophysical properties. The methodology can also be applied to three-dimensional, unsteady, and turbulent flow problems encountered in practical engineering applications.

Another promising direction is the development of adaptive Neural FEM strategies in which the neural network architecture, activation functions, or sampling points are optimized automatically to improve convergence and computational efficiency. Hybrid computational techniques that combine Neural FEM with conventional finite element, finite difference, or spectral methods may further enhance solution accuracy while reducing computational cost.

In addition, future studies may investigate inverse problems and parameter estimation using Neural FEM, enabling the identification of unknown physical parameters directly from experimental or numerical data. The integration of uncertainty quantification and sensitivity analysis into the Neural FEM framework would also improve the reliability of predictions for realistic engineering systems.

Finally, the proposed methodology may be extended to coupled multiphysics problems involving fluid flow, heat transfer, mass transport, electromagnetics, and solid mechanics. Such developments would broaden the applicability of Neural FEM to a wide range of scientific and engineering problems where conventional numerical methods become computationally expensive or difficult to implement.

Chapter 5

Conclusion

In this thesis, a comprehensive numerical investigation of the coupled system of nonlinear ordinary differential equations arising in micropolar fluid is carried out using the Neural FEM. The governing equations are solved by training neural networks to approximate the solution and its derivatives, offering a flexible and efficient alternative to classical numerical methods. The accuracy and reliability of the Neural FEM approach are verified by comparison with solutions obtained using the well-established bvp4c solver, showing excellent agreement across a range of parameter values.

A systematic parametric study is conducted to analyze the influence of key physical parameters on the solution behavior. The results demonstrate that Neural FEM is capable of accurately capturing subtle solution features, including sharp gradients and nonlinear interactions, while providing smooth and continuous approximations. The comparative analysis with bvp4c highlights the effectiveness of Neural FEM in terms of accuracy, convergence, and robustness, particularly in regimes where classical solvers may face challenges due to stiffness or sensitivity to initial guesses.

Overall, this work confirms that Neural FEM is a powerful and reliable tool for solving nonlinear boundary value problems and can serve as a complementary or alternative approach to traditional methods like bvp4c. The insights gained from the comparative study contribute to a deeper understanding of the solution behavior under varying parameters and demonstrate the potential of physics-informed neural network techniques in computational mechanics.

Future research directions may include extending the Neural FEM framework to higher-dimensional or time-dependent problems, incorporating adaptive neural architectures to further enhance accuracy, and exploring hybrid methods that combine classical solvers with neural network-based approximations for improved computational efficiency in complex engineering applications.

Bibliography

[1] John D. Anderson. *"Computational Fluid Dynamics: The Basics with Applications"*. McGraw-Hill, New York, 1995.

[2] Joel H. Ferziger and Milovan Perić. *"Computational Methods for Fluid Dynamics"*. Springer, Berlin, 2002.

[3] Olek C. Zienkiewicz, Robert L. Taylor, and Perumal Nithiarasu. *"The Finite Element Method for Fluid Dynamics"*. Elsevier Butterworth-Heinemann, Oxford, 2005.

[4] Thomas J. R. Hughes. *"The Finite Element Method: Linear Static and Dynamic Finite Element Analysis"*. Dover Publications, New York, 2000.

[5] Maziar Raissi, Paris Perdikaris, and George Em Karniadakis. "Physics-informed neural networks: A deep learning framework for solving forward and inverse problems involving nonlinear partial differential equations". *Journal of Computational Physics*, 378:707, 2019.

[6] George Em Karniadakis, Ioannis G. Kevrekidis, Lu Lu, Paris Perdikaris, Sifan Wang, and Liu Yang. "Physics-informed machine learning". *Nature Reviews Physics*, 3(6):440, 2021.

[7] Khemraj Shukla, Pietro Claudio Di Leoni, James Blackshire, Daniel Sparkman, and George Em Karniadakis. "Physics-informed neural networks for fluid mechanics". *Physics of Fluids*, 32(12):121701, 2020.

[8] I. E. Lagaris, A. Likas, and D. I. Fotiadis. "Artificial neural networks for solving ordinary and partial differential equations". *IEEE Transactions on Neural Networks*, 9(5):1000, 1998.

[9] Pradeep Ramuhalli, Lalita Udpa, and Satish S. Udpa. "Finite-element neural networks for solving differential equations". *IEEE Transactions on Neural Networks*, 16(6):1392, 2005.

[10] Wei Xiong, Xiangyun Long, Stéphane P. A. Bordas, and Chao Jiang. "The deep finite element method: A deep learning framework integrating physics-informed neural networks with the finite element method". *Computer Methods in Applied Mechanics and Engineering*, 436:117681, 2025.

[11] Siddhartha Mishra and Roberto Molinaro. ""Physics-informed neural networks for partial differential equations: A numerical analysis". *IMA Journal of Numerical Analysis*, 42(2):1897, 2022.

[12] Kun Xu and Eric Darve. "Physics constrained learning for data-driven inverse problems". *arXiv preprint arXiv:1807.03415*, 2018.

[13] H. K. Versteeg and W. Malalasekera. *"An Introduction to Computational Fluid Dynamics: The Finite Volume Method"*. Pearson Education, Harlow, UK, 2nd edition, 2007.

[14] A. Cemal Eringen. "Theory of micropolar fluids". *Journal of Mathematics and Mechanics*, 16(1):18, 1966.

[15] T. Ariman, M. A. Turk, and N. D. Sylvester. "Microcontinuum fluid mechanics—a review". *International Journal of Engineering Science*, 11(8): 930, 1973.

[16] A. A. Mohammadein and R. S. R. Gorla. "Heat transfer in a micropolar fluid over a stretching sheet with viscous dissipation and internal heat generation". *International Journal of Numerical Methods for Heat & Fluid Flow*, 11(1):58, 2001.

[17] P. R. Sharma and G. Singh. "Effects of variable thermal conductivity and heat source/sink on MHD flow near a stagnation point on a linearly stretching sheet". *Applied Mathematics and Mechanics*, 30(8):1054, 2009.

[18] Tuncer Cebeci. *"Physical and Computational Aspects of Convective Heat Transfer"*. Springer, New York, 2002.

[19] Uri M. Ascher, Robert M. M. Mattheij, and Robert D. Russell. *"Numerical Solution of Boundary Value Problems for Ordinary Differential Equations"*. SIAM, Philadelphia, 1995.

[20] Lu Lu, Xuhui Meng, Zhiping Mao, and George Em Karniadakis. "DeepXDE: A deep learning library for solving differential equations". *SIAM Review*, 63 (1):228, 2021.

[21] Biswajit Khara, Aditya Balu, Ameya Joshi, Soumik Sarkar, Chinmay Hegde, Adarsh Krishnamurthy, and Baskar Ganapathysubramanian. "NeuFENet: Neural finite element solutions with theoretical bounds for parametric PDEs". 2021.

[22] Sebastian K. Mitusch, Simon W. Funke, and Miroslav Kuchta. "Hybrid FEM-NN models: Combining artificial neural networks with the finite element method". *Journal of Computational Physics*, 446:110651, 2021.

[23] Joel H. Ferziger and Milovan Perić. *"Computational Methods for Fluid Dynamics"*. Springer, Berlin, 4th edition, 2016.

[24] Muhammad Sabeel Khan, Muhammad Asif Memon, Ilyas Khan, and Sayed M. Eldin. "Finite element based direct and iterative approach to investigate a magneto-micropolar flow through a rectangular channel". *Alexandria Engineering Journal*, 75:66, 2023.

[25] Muhammad Sabeel Khan, I. Hameed, M. A. Memon, and E. Bonyah. "Computational analysis of magnetic induced micropolar flow in a rectangular channel through FreeFEM++". *AIP Advances*, 13(4):045106, 2023.

[26] Susanne C. Brenner and Ridgway Scott. *"The Mathematical Theory of Finite Element Methods"*. Springer, New York, 3rd edition, 2008.

[27] Olek C. Zienkiewicz, Robert L. Taylor, and Jian Z. Zhu. *"The Finite Element Method: Its Basis and Fundamentals"*. Butterworth-Heinemann, Oxford, 7th edition, 2013.

[28] Suhas V. Patankar. *"Numerical Heat Transfer and Fluid Flow"*. McGraw-Hill, New York, 1980.

[29] Frank M. White. *"Fluid Mechanics"*. McGraw-Hill, New York, 7th edition, 2011.

[30] Linfeng Li, Jiansheng Xiang, Boyang Chen, Claire E. Heaney, Steven D. Dargaville, and Christopher C. Pain. "Implementing the discontinuous-Galerkin finite element method using graph neural networks with application to diffusion equations". *Neural Networks*, 181:106886, 2025.

[31] Muhammad Sabeel Khan. "A new thermal boundary layer analysis model in the presence of micromagnetorotation within micropolar continuum". *Multiscale and Multidisciplinary Modeling, Experiments and Design*, 8:387, 2025.